Zero-dimensional modeling of unpacked and packed bed dielectric barrier discharges : the role of vibrational kinetics in ammonia synthesis

Zero-dimensional modelling of unpacked and packed bed dielectric barrier discharges:

The role of vibrational kinetics in ammonia synthesis

K. van 't Veer[1,2], F. Reniers[2], A. Bogaerts[1]

[1] *University of Antwerp, Department of Chemistry, Research Group PLASMANT, Universiteitsplein 1, 2610 Wilrijk-Antwerp, Belgium*
[2] *Université Libre de Bruxelles, Faculty of Sciences, Chemistry of Surfaces, Interfaces and Nanomaterials, CP255, Avenue F. D. Roosevelt 50, B-1050 Brussels, Belgium*

Abstract

We present a zero-dimensional plasma kinetics model, including both surface and gas phase kinetics, to determine the role of vibrationally excited states in plasma-catalytic ammonia synthesis. We defined a new method to systematically capture the conditions of dielectric barrier discharges (DBDs), including those found in packed bed DBDs. We included the spatial and temporal nature of such discharges by special consideration of the number of micro-discharges in the model. We introduce a parameter that assigns only a part of the plasma power to the micro-discharges, to scale the model conditions from filamentary to uniform plasma. Because of the spatial and temporal behaviour of the micro-discharges, not all micro-discharges occurring in the plasma reactor during a certain gas residence time are affecting the molecules. The fraction of power considered in the model ranges from 0.005 %, for filamentary plasma, to 100 %, for uniform plasma. If vibrational excitation is included in the plasma chemistry, these different conditions, however, yield an ammonia density that is only varying within one order of magnitude. At only 0.05 % of the power put into the uniform plasma component, a model neglecting vibrational excitation clearly does not result in adequate amounts of ammonia. Thus, our new model, which accounts for the concept in which not all the power is deposited by the micro-discharges, but some part may also be distributed in between them, suggests that vibrational kinetic processes are really important in (packed bed) DBDs. Indeed, vibrational excitation takes place in both the uniform plasma between the micro-discharges and in the strong micro-discharges, and is responsible for an increased N_2 dissociation rate. This is shown here for plasma-catalytic ammonia synthesis, but might also be valid for other gas conversion applications.

Keywords

0D chemical kinetics modelling, global modelling, filamentary plasma, micro-discharges, packed bed reactors, vibrational kinetics, ammonia synthesis

1. Introduction

Ammonia (NH_3) is an important chemical for the manufacturing of various products and is especially crucial in the food industry through its role in fertilizer production [1]. Currently, the Haber-Bosch process is used for NH_3 synthesis. This process is mainly suited for large scale production [2] and has a huge environmental footprint, i.e. approximately 1.2% of the world-wide available energy is consumed for NH_3 synthesis and it produces around 1.5 tons of CO_2 per ton of NH_3, amounting to almost 1% of all greenhouse gas emissions [3].

Recently, plasma technology has gained a lot of attention for efficient alternative and small scale processes. In particular, due to their (operational) simplicity and widespread adoption [4], atmospheric pressure dielectric barrier discharges (DBDs) are a popular plasma source for NH_3 formation from N_2/H_2 gas mixtures. To increase process yields and efficiencies, catalytic packing materials have been introduced in the reactors [5]. In literature, many variations of catalytic material, support and loading arrangements can be found for NH_3 synthesis in DBD reactors, with product yields mostly ranging from 0.1 to 5 % or higher for more complex configurations [5]–[16].

Bai et al. used a powdered catalyst, smeared on the electrode of a DBD, and achieved an NH_3 yield of up to 0.5 %. With increased discharge area, they found higher NH_3 concentrations [8]. Later, they reached a yield of 1.25 % in a micro-gap, at a reduced electric field of ~300 Td. The yield increased with power density, applied voltage and gas temperature. In addition, the discharge frequency was shown to be an important parameter in process optimization [9]. Mizushima and coworkers used a metal-load membrane-like structure as catalyst. A N_2 conversion of up to 2.4 % was reported. When the catalyst was loaded, the NH_3 concentration increased with applied voltage. Without catalyst, this increase was significantly less [10], [11]. Gómez-Ramírez et al. reported their highest N_2 conversion as 2.7 %, corresponding to the smallest discharge gap at constant residence time. They indicate N_2^+ to play an important role in the formation of NH in the gas phase. In addition, electron impact dissociation of NH_3 was indicated as a possible source of NH [12]. Later, they found a N_2 conversion of 7 % and further argued the importance of both the N_2^+ ions and electron impact dissociation of NH_3 [13]. Barboun et al. reported NH_3 yields

up to 2.7 %, depending on the metallic catalyst and the residence time. Higher concentrations were achieved for longer residence times. They separately investigated the influence of bulk gas temperature and plasma input power, and found that a higher input power was more effectively enhancing the plasma-catalytic NH_3 yield than the bulk gas temperature [14]. Peng et al. reached up to 3.7 % NH_3 yield, depending on the discharge frequency, applied voltage, flow rate and gas composition [15]. By optimizing the catalyst support, catalyst material and their manufacturing, as well as the plasma power and electrode configuration, Akay and Zhang reported an NH_3 concentration of 16 % [16].

Packed reactors show beneficial, but complex behaviour. This complexity is due to simultaneous and synergistic effects that can hardly be separated from each other in experimental studies, indicating the need for modelling [17]. Due to the nature of a PB DBD, ideally three-dimensional (3D) modelling is required. However, the computational cost of the latter makes that modelling studies often resort to two-dimensional (2D) or even one-dimensional (1D) geometrical representations to study the plasma physics. As in any chemical process, the chemistry is also an important aspect subject to modelling studies. The potential complexity of the actual molecular chemistries involved again limits the possibilities of 1D and 2D numerical studies due to the computational cost. Instead, such studies are often performed with zero-dimensional (0D) plasma kinetic models.

Babaeva, Kushner and co-workers performed 2D modelling of single and multiple solid particles obstructing the discharge propagation path in humid air mixtures [18]–[21]. Within the same research group, Kruszelnicki et al. reported a reduced version of the same chemistry set for 2D modelling, describing a truer PB configuration [22]. Kang et al. studied the impact of various dielectric barrier arrangements, including a PB reactor in 2D for simple dry air [23], using the methods of Kulikovsky [24]. Similar studies were performed by Russ et al. [25]. Takaki et al. performed both computations and experiments for a N_2 discharge in a PB reactor. They used an analytical description of the electron density and electric field based on 1D approximations [26]. The computed species densities as a function of applied voltage were in agreement with experiments. They also reported the measured vibrational temperature to be constant (around 2250 K) with increasing applied voltage. Thus, they concluded that the additional power at higher applied voltage does not go to vibrational excitation [27], [28]. Mehta et al. also measured significant vibrational temperatures (around 2700 K) in a N_2/H_2 DBD. They suggest that vibrationally excited molecules can play an important role in plasma-catalytic NH_3 synthesis [29], and this was later

substantiated by Rouwenhorst et al. [30]. In our group, Van Laer and Bogaerts performed several modelling studies of PB reactors for various configurations and conditions, operated with helium [17], [31], [32], while Wang et al. developed a model for dry air, focusing on streamer propagation in between the packing beads [33].

The above modelling studies [17]–[27], [31], [32] focussed on the plasma physics rather than the plasma chemistry. The latter was kept simple and did for instance not include excitation to individual vibrationally excited states [17]–[20], [22]–[27], [31], [32].

In some of those studies, various kinds of discharges were observed in PB reactors, such as filamentary discharges and surface ionization waves [22], [33]. Some modelling studies tried to relate single features to specific current peak characteristics [31]. However, experimental current characteristics of PB reactors, with often a far greater number of packing beads compared to modelling configurations, exhibit a complexity not allowing for a distinction between the various kinds of micro-discharges based on the electrical current characteristics [34], [35]. Indeed, the conversion and product yield in PB DBDs are, in general, affected by the various plasma and process parameters and their combinations (e.g. the type of dielectric barrier and its thickness, the packing beads, the discharge frequency, the flow rate, etc.) in complex ways [34], even in reactors without any packing material [35]–[37].

Within our group PLASMANT, several numerical studies have focused on the plasma chemistry in filamentary discharges using 0D modelling, in which filaments were described as sharply peaked power density pulses [38]–[45]. However, the number of micro-discharge pulses in the model and the time between the pulses were chosen rather arbitrary, with motivations based on the discharge frequency alone or in combination with an effective filament discharge volume. In addition, the pulse magnitudes were chosen to mimic the total specific energy input, i.e. the total plasma power, for the sum of all pulses in the model, despite the transient characteristics of filaments, and the plasma power in between the pulses was effectively chosen to be zero. In particular, the importance of the inter-pulse duration was acknowledged [44]. When applied to long time scale simulations, corresponding to the gas residence time, a large number of pulses, in the order of 10,000 to 1 million, was mentioned to occur in the 0D model, for residence times of the order of 1 to 10 s. An agreement with experiments was found, when a power transfer efficiency, i.e. a reduction in power, was introduced [38]. Overall, the 0D models could

achieve good agreement with experiments. The inclusion of vibrational kinetics in a 0D CO_2 DBD model was reported to yield slightly different values, but the overall trends were the same [45].

Colonna et al. performed 0D plasma kinetic studies of repetitive nanosecond pulsed discharges in H_2 [46], and this kinetic description was later used in a similar N_2/H_2 pulsed plasma [47]. The nanosecond pulse repetition was in the order of microseconds. These models included detailed state-to-state kinetics of vibrational levels, or even represented complete collisional-radiative models (i.e. of H_2). Reduction of the vibrational resolution in their models, when compared to the full state-to-state models, showed clearly different vibrational distribution functions [46], [47]. Teramoto and Kim experimentally investigated two consecutive discharge pulses in N_2 [48]. Their results indicate that vibrational excitation in the first pulse influences the second pulse, if it occurs within 300 microseconds of the first pulse [48].

Hong et al. reported on detailed kinetic modelling of NH_3 production related to experimental measurements in a PB DBD, with emphasis (among others) on the vibrational kinetics. The plasma conditions were constant, averaged values, derived from the electrical characteristics. No spatial or temporal behaviour of their PB DBD, mimicking the micro-discharges, was captured in the model. The electron temperature was in the order of 1 to 1.5 eV. A reasonable agreement with experiments was found [49]–[51]. Shah et al. studied NH_3 synthesis in a low pressure radio frequency plasma and succesfully used the same chemistry set to elucidate the underlying reaction mechanisms [52].

To improve upon our past modelling efforts of filamentary discharges in DBD with complex chemistries, we present in this paper an improved and detailed method that more systematically translates the experimental conditions and observations, i.e. the plasma power and the number of micro-discharges, to an equivalent 0D model. This systematic treatment of the number of micro-discharges also allows us to easily capture the difference between regular (unpacked) and PB DBDs. More specifically, we study the influence of the power deposition in between filamentary pulses and the role of vibrationally excited species.

We describe the computational methods in Section 2, including the plasma kinetics model (2.1), the chemistry (2.2), the reduced electric field calculation (2.3) and a description of the concepts introduced in our model concerning the plasma power (2.4). The plasma and surface chemistry is presented in full in Appendix A and B,

respectively. In Appendix C we include a more detailed description of the treatment of plasma power in our model. Section 3 presents the results, including the NH_3 density evolution (3.1), the reaction mechanisms (3.2) and important calculated plasma parameters, such as the reduced electric field and vibrational temperature (3.3), followed by the conclusions (Section 4).

2. Computational Methods

2.1. Plasma kinetics model

We used the zero-dimensional plasma kinetics solver ZDPlasKin [53], coupled to the BOLSIG+ [54] numerical solver of the steady state Boltzmann equation for electrons. The plasma kinetics solver solves the continuity equations for the various species p with number density $n_p(t)$

$$\frac{dn_p}{dt} = \sum_r c_{r,p} k_r \prod_q n_q \tag{1}$$

where $c_{r,p}$ is the stoichiometry number of species p in reaction r, k_r is the rate coefficient and q are the colliding species in reaction r. The rate coefficients, k_r, are either taken from literature, often as a function of the gas or electron temperature, or they are evaluated from electron impact cross sections and the electron energy distribution function (EEDF) through BOLSIG+. The EEDF calculation with BOLSIG+ requires an electric field as input. The EEDF returns the mean electron energy at which the rate coefficients are evaluated.

The total number density of gas phase species can increase with time, e.g. due to dissociation, in turn increasing the pressure. After each time progression, we modify all gas phase species densities to return the set (atmospheric) pressure. This changes the mass density such that it is no longer the initial value. For any calculation involving initial densities and new densities (after modification), the new densities are normalized to the initial value such that the mass density is the same. Both the modification and normalization are assumed linear, i.e. an equal multiplication factor is applied for all gas phase species.

2.2. Plasma and surface chemistry included in the model

N_2, H_2, their corresponding atoms, ions and vibrationally and electronically excited states, as well as various compound species, empty surface sites and surface adsorbed species, are considered in the plasma chemistry, as listed in Table 1. We have used a 75/25% N_2/H_2 ratio as input gas. It should be noted that this ratio does not correspond to the stoichiometry of NH_3. Indeed, in plasma catalysis, the use of more N_2 can be beneficial for NH_3 synthesis because N_2 is more difficult to dissociate compared to H_2, requiring more than twice the electron energy, i.e., the threshold for electron impact dissociation of N_2 is ~9.8 eV, while it is 4.5 eV for H_2 [55].

Table 1. The species taken into account in the plasma and surface kinetics. Surface adsorbed species are indicated by (s).

	Nitrogen	Hydrogen
Ground states	N_2	H_2
	N	H
	NH, NH_2, NH_3	
Vibrationally excited states	$N_2(V = 1 \dots 24)$	$H_2(V = 1 \dots 3)$
Electronically excited states	$N_2(A^3\Sigma_u^+), N_2(B^3\Pi_g),$	$H_2(b^3\Sigma_u^+), H_2(B^1\Sigma_u^+),$
	$N_2\left(a'^1\Sigma_u^-\right), N_2(C^3\Pi_u)$	$H_2(c^3\Pi_u), H_2\left(a^3\Sigma_g^+\right)$
	$N(^2D^0), N(^2P^0)$	
Ions	N^+, N_2^+, N_3^+, N_4^+	H^+, H_2^+, H_3^+
		H^-
	$NH^+, NH_2^+, NH_3^+, NH_4^+, N_2H^+$	
Surface adsorbed species	$N(s)$	$H(s)$
	$NH(s), NH_2(s)$	

The reactions involving only N_2 related species are taken from a revised chemistry set recently developed in our group for modelling a gliding arc plasma, which also operates at atmospheric pressure, and was updated from [56]. It now includes a detailed description of the vibrational kinetics of N_2, considering 24 vibrational states (based on resonant vibrational excitation cross sections available from the Phys4Entry database [57]) and describing the N_2-N_2 vibrational-vibrational (VV) exchanges, N_2-N_2 vibrational-translational (VT) relaxations [58], and N_2-N VT relaxations, with single and multi-quantum transitions [59]. The reactions involving only H_2 and both N and H components are adopted from Hong et al. [49]. They also include the vibrational states of H_2, considering 3 levels, and H_2-N_2, H_2-H_2, H_2-N and H_2-H VT relaxations, as well as H_2-H_2 and N_2-H_2 VV exchanges (involving the first 8

vibrational levels of N_2). A full list of the included reactions, as well as all the processes involving vibrational levels, is included in Appendix A.

The surface kinetics are also adopted from Hong et al. [49] and include direct adsorption, dissociative adsorption, recombination desorption, elementary Eley-Rideal and Langmuir-Hinshelwood reaction steps, and surface relaxation of excited states. The calculated rate coefficients represent a metallic surface, but we do not consider different materials in this study. Indeed, we do not consider here the influence of the catalytic material, i.e., the surface kinetics model is based on sticking probabilities and their values are not known for a wide variety of materials. This was indeed not the focus of this paper and would require other type of modelling (i.e., microkinetics modelling based on transition state theory and density functional theory data [29]). In contrast, in this paper we investigate the role of vibrational excitation in a DBD applied to a plasma-catalytic process, for which we simply assume a metallic surface (without further specification). A detailed description of the surface kinetics model is given in Appendix B. The sticking probabilities in the model are specific for the different vibrationally excited states, where applicable.

2.3. Calculation of the electric field

The electric field E, at which BOLSIG+ solves the Boltzmann equation [54], is calculated using the differential form of the Joule heating equation

$$\frac{dP}{dV} = \mathbf{J} \cdot \mathbf{E} = \sigma E^2 \tag{2}$$

where P is the power and dV a volume element, $\mathbf{J} = \sigma\mathbf{E}$ is the current density and σ is the electron conductivity. Assuming no spatial dependence, the reduced electric field (E/N) can be calculated from the power density $p \equiv P/V$ as

$$\left(\frac{E}{N}\right) = \frac{1}{N}\sqrt{\frac{p}{\sigma}} \tag{3}$$

where N is the total number density of gas phase species. The electron conductivity is calculated by

$$\sigma = en_e\mu_e \tag{4}$$

where e is the elementary charge, n_e the electron number density and μ_e the electron mobility, calculated by BOLSIG+.

2.4. Power definition in the model

In our model, we defined the power density as a function of time. This function allows us to include the concept of micro-discharges in the 0D model. A proper translation of experimentally observed micro-discharges allows us to systematically describe the plasma conditions found in both packed bed (PB) and non-packed DBD reactors. The term micro-discharges is used rather than filaments, because experimental current characteristics do not reveal the specific type of discharge that took place [34]. We model the individual micro-discharges as triangular power density pulses with a certain duration (i.e. width or life time). Such power density pulses have already been shown to return electron avalanches [42], [44].

DBDs typically operate with low gas flow rates (order of 100 mL/min). We consider the residence time of molecules in the reactor to be greater than a single discharge period. Thus, it takes multiple discharge cycles for the molecules to pass through the reactor. During one half discharge period, we can count the number of micro-discharges, e.g. from the measured current characteristics [35]. If we assume that those micro-discharges are distributed uniformly throughout the whole plasma reactor, it is obvious that, within one discharge period, the molecules entering the reactor cannot have seen all micro-discharges that took place, simply because the molecules have not crossed the whole reactor yet. In other words, during a certain residence time, millions of micro-discharges can occur throughout the reactor, but it is impossible for a single molecule to be exposed to all of them. This means that the plasma power deposited into the plasma reactor through the micro-discharges is not deposited to every single molecule in the reactor. Thus in our model, we do not by definition consider the total experimental plasma power, because we do not consider all micro-discharges that occur throughout the whole reactor within a certain residence time.

In addition, we introduce the concept of a uniform plasma component. By doing so, we distinguish between power deposited by the micro-discharges (i.e. strong plasma, temporally and spatially isolated in nature) and power

deposited by a uniform or homogenous plasma (i.e. weaker plasma that is always present, throughout the whole reactor and continuous through time). Typically, both in experiments and modelling, it is assumed that all power is deposited by the micro-discharges [34], [38]–[45]. In our present model, we scale the plasma from a filamentary to a uniform plasma. To do this, we have introduced a power density distribution factor, γ, when defining our time-dependent power density function. This parameter is used to set the minimum power density p_{min} based on the maximum power density p_{max}, i.e. $p_{min} = \gamma p_{max}$. See Appendix C.1 for further details.

Figure 1 shows the power included in our model, due to the micro-discharges alone and the total power, as a function of γ. We consider 200 micro-discharges per discharge half cycle (i.e. the original value from the adopted plasma parameters used in our model [60]) as well as 50 micro-discharges (i.e. a reduced number, because the number of micro-discharges in N_2 is typically lower than in other reactive gases).

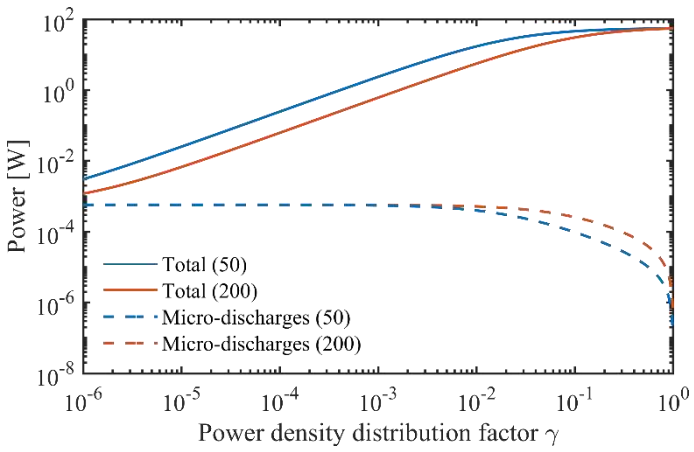

Figure 1. Total power and power due to the micro-discharges used in the model based on 55 W of plasma power determined from experiments [35], as a function of the power density distribution factor γ, both for 200 and 50 micro-discharges per half cycle (indicated in brackets in the legend). See Appendix C for details.

Figure 1 shows that for the most filamentary plasma considered ($\gamma = 10^{-6}$), we use very little power in the model (3 mW and 1.2 mW for 50 and 200 micro-discharges per half cycle, respectively). As the plasma becomes more uniform (γ towards 1), the power increases up to 55 W for a fully uniform plasma ($\gamma = 1$), that is, the total plasma power as experimentally determined. In any case, the total power is always determined by the uniform plasma component. Indeed, the power in the model due to micro-discharges is very low, because we do not consider all the micro-discharges that occur throughout the whole reactor during a certain residence time, but rather the micro-discharges that individual molecules could be exposed to (on average) during their residence time in the reactor, as explained above.

To summarize, we are modelling a control volume which is moving through a (packed bed) reactor at the flow velocity. The probability that a micro-discharge occurs in this control volume is given by the fraction of micro-discharges, which can be calculated from the reactor volume traversed by the gas during one discharge period divided by the total reactor volume. The plasma power density is determined from the plasma power and the typical volume of the micro-discharges (see Appendix C.2). We apply our model to a plasma power of 55 W, a discharge frequency of 28.6 kHz and a micro-discharge life time of 15.6 ns, adopted from experiments [35]. We assume a constant gas temperature of 400 K and atmospheric pressure. We consider 200 micro-discharges per half cycle [60], as well as 50, for which the micro-discharges occur every 16 ms and 66 ms, respectively (based on a residence time of 3.33 s).

As an example, for 50 micro-discharges per half cycle, after the above considerations, the power density ranges from a minimum value, p_{min}, of 2.5 W/cm^3 and a maximum value, p_{max}, of 2.5×10^6 W/cm^3 as used in the most filamentary plasma ($\gamma = 10^{-6}$), to a constant value of 5.5×10^4 W/cm^3 in the fully uniform plasma ($\gamma = 1$).

We believe that assuming a constant gas temperature of 400 K is a valid approach to represent the average plasma temperature in the reactor, despite the fact that the formation of NH_3 is exothermic, meaning that the gas would heat up if NH_3 is created. From our experimental experience, we do not observe a significant temperature increase with the formation of NH_3. This can be explained by the low gas flow rate and cooling of the gas at the reactor walls.

Finally, we believe that the concepts introduced into our new model allow for a systematic translation of experimental conditions to the model, based on the number of micro-discharges, their life time and the gas residence time in the reactor, so that we can for instance also distinguish between regular and PB DBDs. This is discussed in further detail in Appendix C.3.

3. Results and discussion

We ran a large number of calculations (all of which are based on the same plasma power (55 W)), which we provide in the supplementary information. Here we present selected data for 50 and 200 micro-discharges per half cycle (for which the volume, and thus the power density, differs by a factor 4). We considered the following power density distribution factors: 10^{-6}, 10^{-5}, 10^{-4}, 10^{-3}, 10^{-2}, 10^{-1} and 1 (10^{0}).

3.1. Species density evolution and steady-state densities

Initially we consider three types of models: (i) the full model, including vibrational kinetics with the power density described in section 2.3; (ii) the same model without vibrational excitation (i.e., neglecting processes A3 and A4 and disregarding all processes in Appendix A and B that involve vibrational levels); and (iii) the full model of (i), but considering only the uniform power density component, i.e., assuming no micro-discharges, but simply the uniform DBD plasma (that is, neglecting the triangular power density pulses on top of the constant value). For model (iii) the power density distribution factor thus represents uniform plasma of various intensity.

The various models and conditions (which are all derived from the same plasma power) provide a somewhat different NH_3 density time evolution, as illustrated in Figures 2 - 4 for a selection of the calculations, mainly focussing on 50 micro-discharges per discharge half cycle. The distinct conditions (i.e. the various power density distribution factors, γ) are reported in Figures 2, 3 and 4 with unique and consistent colours. In Figure S1 – S3 we plot the calculated NH_3 density as a function of time for a larger variety of number of micro-discharges, showing that the observed trends are valid over a larger range of conditions.

Figure 2 shows the full model results. The more uniform plasma (larger γ) reaches steady state NH_3 densities very quickly (i.e. after 16 ms for $N_{MD} = 50,\ \gamma = 10^{-3}$) or almost immediately (i.e. after 0.53 ms for $N_{MD} = 50,\ \gamma = 10^{-1}$), but the most uniform plasma ($\gamma = 10^{-1}$) reaches a lower steady state value. The more filamentary plasma ($\gamma = 10^{-4}$ and 10^{-6}) reaches a steady state on much longer time scales, and not necessarily within the gas residence time (3.33 s). Generally, a steady state NH_3 density is reached earlier when the plasma becomes more uniform ($N_{MD} = 50,\ \gamma = 10^{-4}$ compared to $N_{MD} = 50,\ \gamma = 10^{-6}$). In addition, more micro-discharges ($N_{MD} = 200,\ \gamma = 10^{-4}$ vs. $N_{MD} = 50,\ \gamma = 10^{-4}$) yield higher NH_3 densities and steady state is reached later. The latter is attributed to the shorter inter-pulse times. Indeed, this makes it more likely for a pulse to

be influenced by the previous pulse, because of a relatively large number of created radicals still being present. The steady state value is in principle determined by the surface reactions and electron impact dissociation of NH_3, which is an important NH_3 loss process (see section 3.2). Finally, the most pronounced filamentary plasma, that reaches steady state slowly ($N_{MD} = 50,\ \gamma = 10^{-6}$) can reach higher steady state NH_3 densities than the more uniform plasmas ($N_{MD} = 50,\ \gamma = 10^{-3}$ and 10^{-1}).

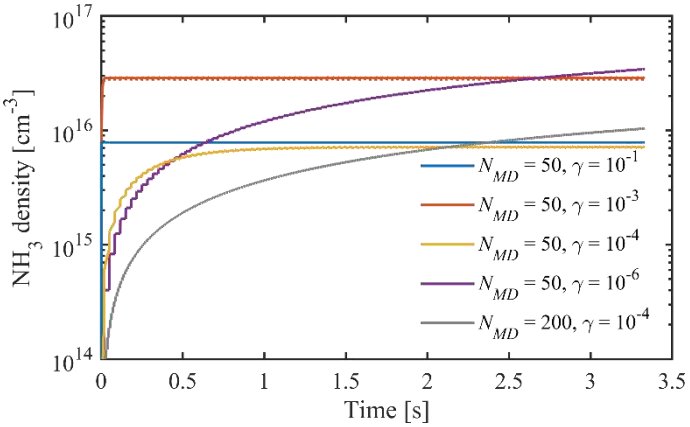

Figure 2. NH_3 density evolution as a function of time for selected conditions of γ and N_{MD}, obtained with the full model (i).

Figure 3 compares the full model (model (i)) with the model neglecting vibrational excitation (model (ii)). The most filamentary plasma can reach the highest NH_3 density if vibrational excitation is present ($N_{MD} = 50,\ \gamma = 10^{-6}$: compare (i) vs. (ii)). Those conditions did not yet reach steady state in the full model (i), whereas a lower steady state NH_3 density is already reached if vibrational excitation is not included (model ii). When the plasma becomes only slightly less filamentary ($\gamma = 10^{-5}$ compared to $\gamma = 10^{-6}$), the NH_3 density cannot reach an adequate steady state value anymore without vibrational excitation (model (ii): $N_{MD} = 50,\ \gamma = 10^{-5}$ compared to $\gamma = 10^{-6}$). When comparing the number of micro-discharges in model (ii) ($N_{MD} = 200,\ \gamma = 10^{-5}$ against $N_{MD} = 50,\ \gamma = 10^{-5}$), we observe in Figure 3, similar to Figure 2, that a larger number of micro-discharges can surpass the steady state NH_3 density obtained with less micro-discharges for the same γ value. Finally, by comparing models (i) and (ii) for $N_{MD} = 50,\ \gamma = 10^{-5}$, the results further indicate that vibrational excitation yields a higher steady state NH_3 density. Thus, Figure 3 demonstrates that vibrational excitation does contribute towards reaching high NH_3 yields in filamentary plasma ($\gamma = 10^{-6}$ and $\gamma = 10^{-5}$).

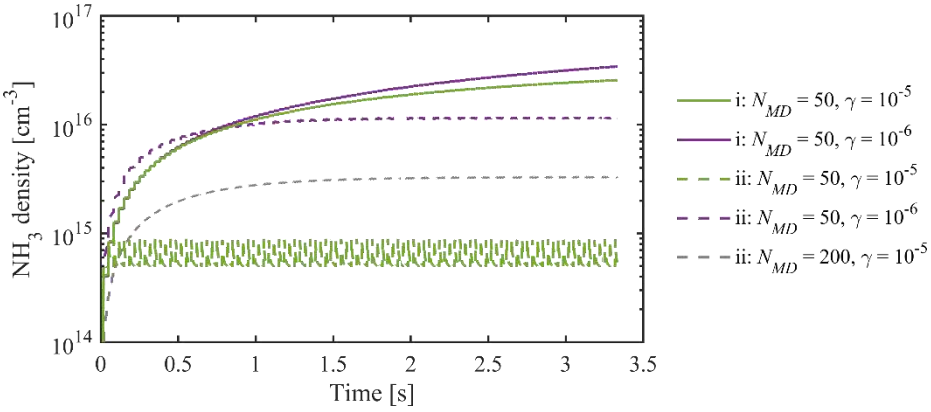

Figure 3. NH_3 density evolution as a function of time for selected conditions and comparison of the full model (model (i), solid lines) and the model neglecting vibrational excitation (model (ii), dashed lines).

Figure 4 compares the full model (model (i)) with the model neglecting the micro-discharges (model (iii)), assuming 50 micro-discharges per discharge half cycle. For $\gamma = 10^{-3}$, both models overlap, indicating that the micro-discharges in model (i) were not strong enough to influence the NH_3 formation. For the most filamentary plasma ($\gamma = 10^{-6}$), the strong micro-discharges are very important for the formation of NH_3. In intermediate plasma ($\gamma = 10^{-4}$), the micro-discharges only slightly elevate the NH_3 yield. Thus, based on Figure 4 we can consider $\gamma \geq \sim 10^{-3}$ as uniform plasma and $\gamma = 10^{-6} \ldots \sim 10^{-4}$ as filamentary plasma.

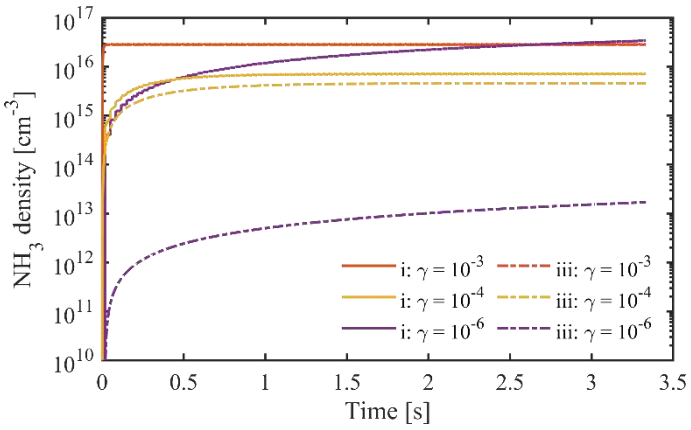

Figure 4. NH_3 density evolution as a function of time for selected conditions, and comparison of the full model (model (i), solid lines) and the model neglecting the micro-discharges (model (iii), dashed lines). All data is from calculations assuming 50 micro-discharges per discharge half cycle (N_{MD}). The results of model (i) and (iii) for $\gamma = 10^{-3}$ overlap each other.

Combining the comparisons made in Figure 3 and 4, we can conclude that despite being in the filamentary regime ($\gamma = 10^{-6} \ldots \sim 10^{-4}$), both the micro-discharges (cf. Figure 4) and the vibrationally excited states (cf. Figure 3) actively contribute to the NH_3 formation.

In Figure 5, we plot the final NH_3 density resulting from the three models, for 50 micro-discharges, over the full range of filamentary, intermediate and uniform plasma (i.e. as a function of γ). In the full model, we observe a slight drop in the NH_3 density at $= 10^{-4}$,. Similar behaviour was also observed for the other number of micro-discharges (cf. Figure D.4(a)). After comparing models (i) and (iii) in Figure 5, we attribute this behaviour to a possible change in mechanics that govern the steady state, because the micro-discharges do not influence the NH_3 density evolution beyond $\gamma = 10^{-3}$ (cf. model (i) and (iii) in Figure 4).

Clearly, in the filamentary range ($\gamma = 10^{-6}$ ... ~10^{-4}), there is a synergistic effect between the micro-discharges and vibrational excitation, because the sum of the results of model (ii) and (iii) is less than model (i). This can be understood because in model (iii) the N formation is enhanced through a higher effective rate coefficient of N_2 dissociation, due to the vibrationally excited states compared to dissociation from the ground state, while in model (ii) the N formation is enhanced through a higher electron density, due to the micro-discharges compared to an uniform plasma (see also Section 3.2, Figure 6). As these two effects are combined in model (i), it yields a more than linear increase relative to model (ii) and (iii).

In addition, it should be noted that the final NH_3 density obtained in model (i) does not significantly vary (i.e., less than an order of magnitude) for all conditions, despite significantly different – including very low – amounts of power being used in the model (cf. Figure 1). This observation potentially explains why Hong et al. found reasonable agreement with PB DBD experiments for their 0D model that included the interactions of the vibrational states, but assumed a uniform plasma [49] (i.e. corresponding to $\gamma = 10^0 = 1$ in the present study).

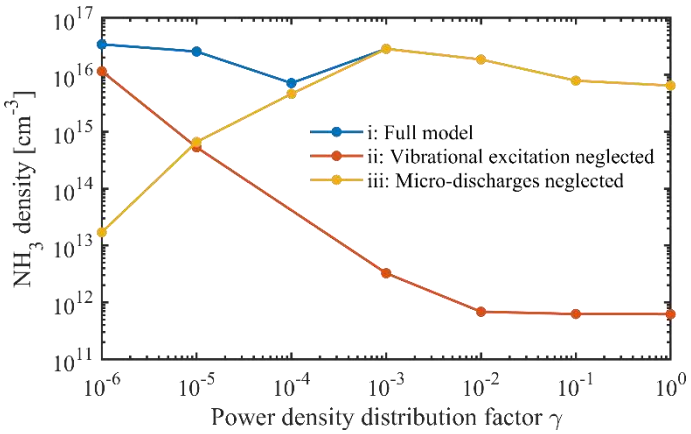

Figure 5. Final (steady state) NH_3 density as a function of γ, for 50 micro-discharges per discharge half cycle, as calculated in the full model (i), when neglecting vibrational excitation (model (ii)), and when neglecting micro-discharges (model (iii)).

The NH_3 yield (defined here as the final calculated NH_3 density divided by the theoretical NH_3 density if 100% of the initial gas would be converted to the product) in the most filamentary case ($\gamma = 10^{-6}$) is calculated as 1.11 %. Compared to literature, where NH_3 yields between 0.1 and 5 % were reported for plasma-catalytic NH_3 synthesis in PB DBDs (cf. the overviews in [5]–[7]), 1.11 % is a reasonable value, but can be considered on the lower side. This is not unexpected, as we present here a more fundamental study, not focusing on maximum NH_3 yields by using appropriate catalysts. In addition, not all models reached steady state already, at the considered residence time of 3.33 s, and thus the maximum possible yield might not have been reached (especially for the full model (i), cf. Figure 2 and Figure S4). Moreover, the experimental conditions, and specifically the plasma power of 55 W adopted in the present study, can be considered low, as this value was adopted from previous modelling and experimental studies [35], [60] of CO_2 plasma. The ionization threshold of N_2 is higher (~15.6 eV compared to ~13.8 eV for CO_2) and it also has a slightly higher dissociation threshold (~9.8 eV [55] compared to ~7 eV for CO_2 [60]), so that a higher power might be needed to reach higher NH_3 yields. In the future we will investigate how to improve the NH_3 production, based on this model. Still, our calculated values are in the same order of magnitude as in the experiments from literature, suggesting that our model could provide a reasonable description of NH_3 synthesis in a (packed bed) DBD, and stressing again the importance of including vibrational excitation.

3.2. Reaction mechanisms

A reaction analysis did not reveal clear differences between the actual reactions taking place for the different model assumptions and conditions. However, we gained some global insights. In Figure 6 and 7, the species densities, both in the plasma phase (electrons, N, H, NH, NH_2, NH_3, $N_2(V)$), and at the surface (N(s), H(s), NH(s) and NH_2(s)) are plotted as a function of time. The surface-adsorbed species in fact represent the surface coverages of these species. We present the results of the full model (i), with 50 micro-discharges per half cycle and the most filamentary plasma (i.e. $\gamma = 10^{-6}$). Generally we see that the micro-discharges, because of their ns time scale, cause pulsed behaviour in the neutral and surface-adsorbed species densities, with pulses of ms widths. This is true for most species, including the vibrationally excited states of N_2, for which the density rises by approximately one order of magnitude (see further discussion below).

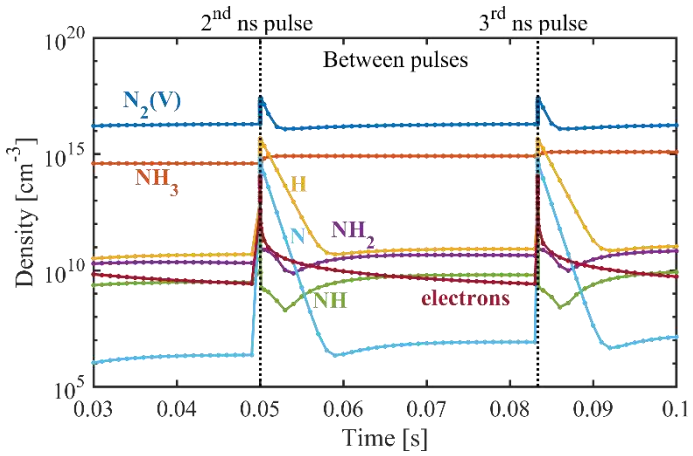

Figure 6. Gas phase species density evolution with time, for the 2nd and 3rd micro-discharge pulse, obtained for 50 micro-discharges per half cycle in the full model (i) and the most pronounced filamentary plasma ($\gamma = 10^{-6}$). The two ns micro-discharge pulses are indicated, but are not resolved in detail on this long time scale.

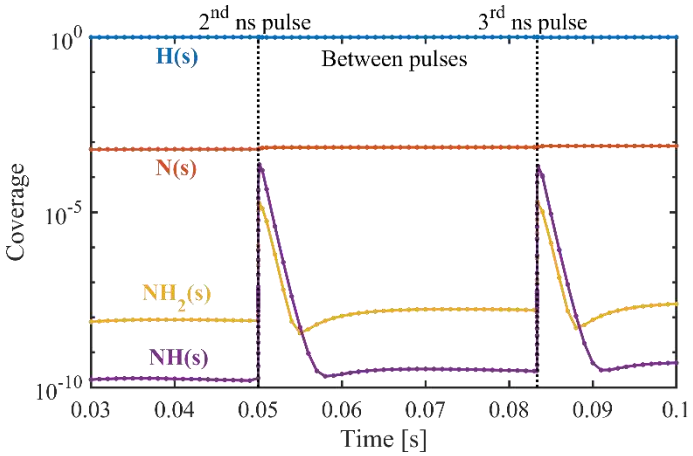

Figure 7. Surface coverages, calculated from the surface species densities, as a function of time, over the 2nd and 3rd micro-discharge pulse, obtained for 50 micro-discharges per half cycle in the full model (i) and the most pronounced filamentary plasma ($\gamma = 10^{-6}$). The two ns micro-discharge pulses are indicated, but are not resolved in detail on this long time scale.

In our model we see that the surface quickly becomes covered with H(s), due to dissociative adsorption of H_2. In the micro-discharges, the electron density increases rapidly due to ionization of both N_2 and H_2, and in addition N_2 and H_2 are dissociated by electron impact. The dissociation products have a relatively long lifetime until after the micro-discharge (cf. Figure 6). During the uniform plasma in between the micro-discharges, we observed the formation of NH_3, basically by a two-step process, starting after the micro-discharge. First NH(s) is formed through an Eley-Rideal mechanism (reaction of N with H(s)). Then, NH_3 is formed through an additional Eley-Rideal step (reaction of NH(s) with H_2). During the micro-discharges, NH_3 is actually lost due to electron impact dissociation. The main dissociation products are NH and NH_2, which also remain present until after the micro-discharge. NH reacts with H(s) (Eley-Rideal step) into NH_2(s), and subsequently NH_3 can be formed (Langmuir-

Hinshelwood step with H(s)). In addition, also NH_2 reacts with H(s) into NH_3 (Eley-Rideal). H atoms created from electron impact dissociation of H_2 in the micro-discharges are converted back to H_2 after the micro-discharge by desorption (i.e. Eley-Rideal step with H(s)).

Clearly, the observed mechanisms are dictated by the quick surface coverage by H(s). It should however be noted that our surface kinetics model (Appendix B) contains several input data subject to uncertainties, so the above analysis is only qualitative. A more detailed quantitative examination of the various reaction steps would require microkinetics modelling based on transition state theory and density function theory calculations, which is beyond the scope of present study.

3.3. Reduced electric field and vibrational temperatures

To gain more insight into the various electron impact processes, we plot in Figure 8 the electron energy loss fractions for vibrational excitation, dissociation and ionization of N_2 as a function of the reduced electric field (E/N). Vibrational excitations are the main electron impact processes at a weak reduced electric field (E/N = 1 to 30 Td), and especially vibrational excitation of N_2(V) towards higher vibrational levels is important. However, the tail of this process does not fall off sharply upon rising E/N, and vibrational excitation is still present towards E/N = 100 Td. The ionization processes and the dissociation of N_2 through vibrationally excited states, more or less, overlap with each other.

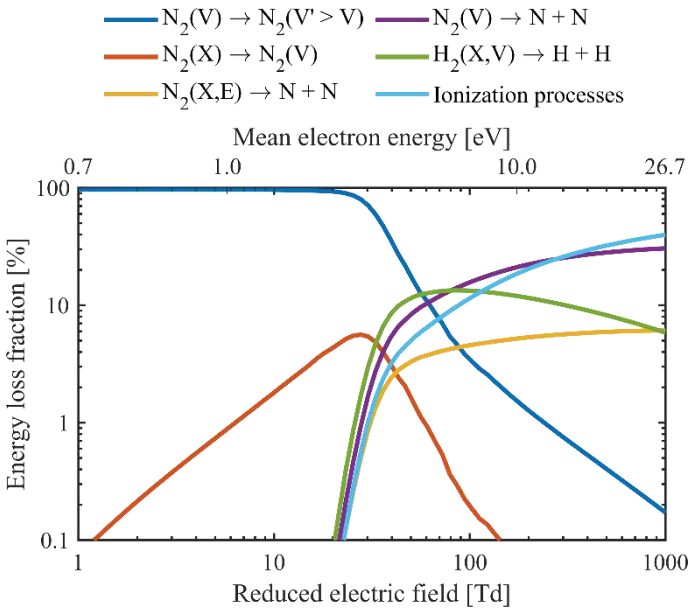

Figure 8. Fractions of electron energy transferred to various important electron impact collisions (i.e. vibrational excitation, dissociation and ionization) in a N_2/H_2 75/25 % mixture at 400 K, as a function of the reduced electric field, calculated using BOLSIG+ [54] from the corresponding cross sections. The ionization processes include direct and dissociative ionization of various molecules (N_2, H_2, NH, NH_2 and NH_3) as well as direct ionization of the atoms (N and H), not only from the ground levels, but also from the vibrationally and electronically excited levels of N_2 and H_2. Vibrational excitation of H_2 is not plotted as it has an electron energy loss fraction less than 0.1 %. The mean electron energy, evaluated from the EEDF at each reduced electric field, is reported on the top x-axis. The cross sections used for vibrational excitation of N_2 and H_2 are the resonant vibrational excitation cross sections [57], [61], [62] taken from the Phys4Entry database, for which 38 and 9 levels are taken into account, respectively. The notations (X), (V) and (E) denote the ground state, vibrational levels and electronic excited levels, respectively.

In Figure 9, we plot the reduced electric field E/N and the vibrational temperature T_V as a function of time, before and after the 2nd and 3rd micro-discharge pulse (conditions: 50 micro-discharges per half cycle and $\gamma = 10^{-6}$). The vibrational temperature is calculated from the first vibrational level and the ground state, by

$$T_V = \frac{E_1 - E_0}{\ln(n_0/n_1)} \tag{5}$$

where E is the energy of the vibrational level and n the corresponding number density. The subscripts indicate the ground and first vibrationally excited state.

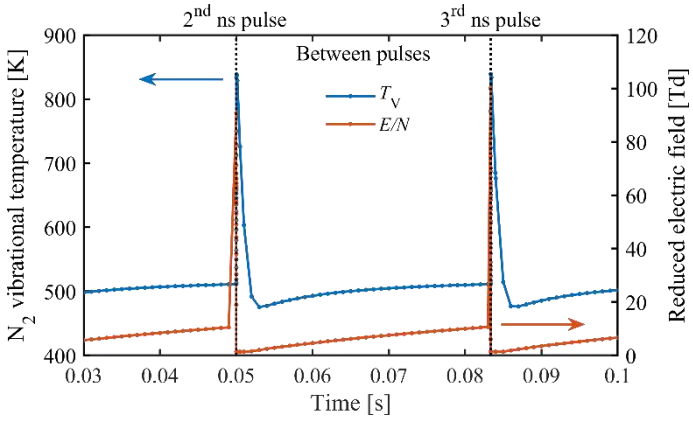

Figure 9. N_2 vibrational temperature (left y-axis) and reduced electric field (right y-axis) as a function of time, for the 2nd and 3rd micro-discharge pulse, for 50 micro-discharges per half cycle in the full model (i) and the most filamentary plasma ($\gamma = 10^{-6}$). The two micro-discharges with ns pulse width are indicated, but are not resolved in detail on this long time scale.

Figure 9 shows that the reduced electric field peaks sharply during the micro-discharge pulses, as expected. The vibrational temperature increases as well, but it decreases more slowly over a few milliseconds. From Figure 8 we can deduce that vibrational excitation is dominant in between the micro-discharge peaks (where E/N is in the order of 1 to 10 Td), but also occurs during the micro-discharges (with E/N around 100 Td; especially when considering that the maximum electric field is not reached instantaneously). Figure 6 also indicated a small rise in vibrationally excited N_2 density during the micro-discharges, as mentioned before. The rising E/N in between the micro-discharges can be understood from the constant power density, and the drop in electron density (due to recombination and lack of ionization, cf. Figure 6 and 8) and Equation 3 and 4, from which follows $E/N \propto 1/\sqrt{n_e}$.

Figure 10 shows the maximum and minimum (steady state) reduced electric field (E/N) over the full range of filamentary to uniform plasma, for 50 micro-discharges per half cycle, obtained from the full model. E/N is greater than 100 Td (i.e. ~140 Td) inside the micro-discharges (maximum values), and 1 to 10 Td in between the micro-discharge pulses (minimum values), in the filamentary plasma regime ($\gamma = 10^{-6} \ldots 10^{-4}$), but the value inside the micro-discharges drops upon increasing γ, because the power is more evenly spread in the entire plasma reactor and not only concentrated in the micro-discharges. Figure 10 further justifies our identification of $\gamma \geq \sim 10^{-3}$ as intermediate and uniform plasma, and $\gamma = 10^{-6} \ldots 10^{-4}$ as filamentary plasma, which was based on Figures 2 - 4 (see Section 3.1). In between the micro-discharges the opposite trend occurs, showing a rise in E/N upon increasing γ, again because the power is more evenly spread in the entire plasma reactor, thus increasing the field strength of the uniform plasma component. Indeed, the electric field is calculated from the power density (see

Eq. 3), so the non-zero power density in between the micro-discharges (when $\gamma > 0$) yields a non-zero electric field as well.

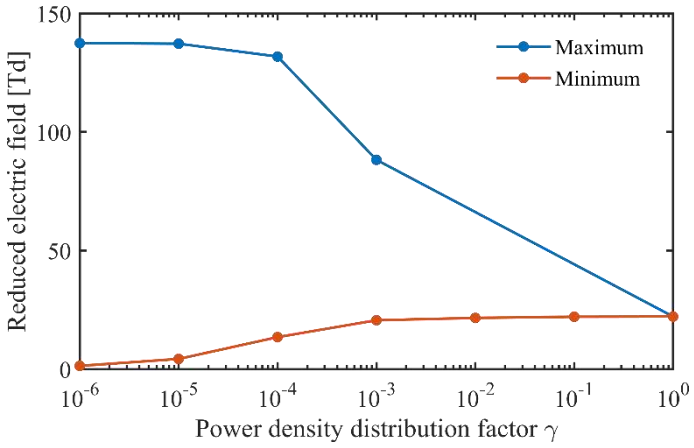

Figure 10. Maximum (i.e., during the micro-discharges) and minimum (i.e., in between the micro-discharges) reduced electric field, in steady state, as a function of γ, for 50 micro-discharges per discharge half cycle, as calculated in the full model (model (i)).

Figure 11 shows the vibrational temperature, again as a function of the plasma uniformity (γ) for 50 micro-discharges per half cycle, obtained from the full model. The values during and in between the micro-discharges show a similar trend as a function of γ, but the vibrational temperature during the micro-discharges is slightly higher. This indicates that vibrational excitation indeed occurs during the micro-discharges. The maximum difference is 900 K (for $\gamma = 10^{-4}$). In the filamentary regime ($\gamma = 10^{-6} \ldots 10^{-4}$) the vibrational temperature reaches values up to 2500 K. In literature, N_2 vibrational temperatures of experimental (PB) DBDs are reported in the order of 1750 to 3000 K [28], [29], hence in reasonable agreement with our calculations. However, as the modelling conditions are not exactly the same (which was not the purpose of this study), we cannot quantitatively compare with those studies.

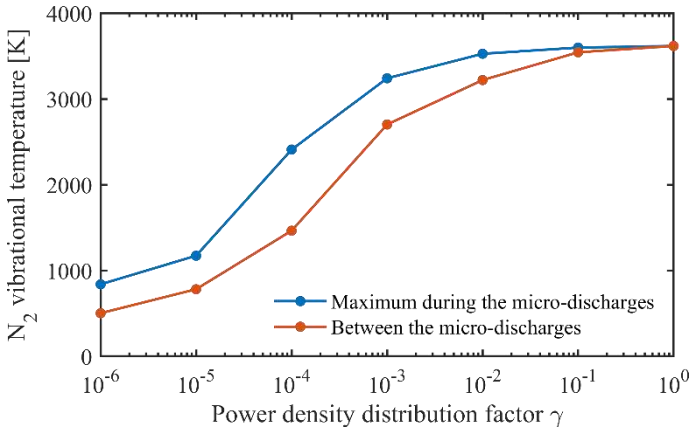

Figure 11. Maximum N_2 vibrational temperature during the micro-discharges and vibrational temperature in between the micro-discharge pulses (cf. Figure 9), as a function of γ, for 50 micro-discharges per half cycle, as calculated in the full model (model (i)).

The gas kinetic temperature in the DBD is assumed to be 400 K. Thus, Figures 8 - 11 indicate that vibrational excitation is generally strong enough to cause a significant vibrational-translational non-equilibrium, both inside the micro-discharges and in the uniform plasma. At the same time, because of the low gas kinetic temperature, loss of the vibrational populations by VT relaxation is limited [63].

In general, we can conclude that the vibrational temperature is significant in both the micro-discharges and the uniform plasma, as long as not all the power is assigned to the micro-discharges, thus stressing again the importance of vibrational excitation for NH_3 synthesis in a (PB) DBD, both during the micro-discharges and in between them.

4. Conclusions

We presented a new method for describing micro-discharges in DBDs, including packed bed DBDs, in a zero-dimensional plasma kinetics model, by describing the spatial and temporal nature of these micro-discharges or filaments in a more systematic way. This approach allows capturing the properties of both packed bed and unpacked DBD reactors, mostly through the number of micro-discharges taking place and the power considered in the model. Indeed, due to the spatial and temporal isolated nature of micro-discharges in DBDs, molecules entering the plasma reactor cannot see all the micro-discharges taking place during one discharge cycle within the full reactor, simply because the molecules do not traverse the whole reactor within this time period. Thus we did not automatically consider the total experimental plasma power in our model. We scaled our models over a wide range of plasmas, i.e. from filamentary to uniform plasmas, by redistributing the power. This was done by systematically changing

the time-dependent power density function in our model. Due to the relatively short duration of the micro-discharges, the considered power in the model is mostly determined by the power in the uniform plasma component.

When we included vibrational excitation, our calculated final NH_3 density did not vary to a large extent (i.e., within one order of magnitude), despite the fact that the power assumed in the model varied over many orders of magnitude, mimicking the full range from filamentary to uniform plasma. Note that we only considered up to 0.447 % of the experimental plasma power in the filamentary model, of which up to 0.446 % is assigned to the uniform plasma component, and 0.001 % to the micro-discharges, because individual molecules cannot see all the micro-discharges taking place within their residence time in the reactor.

By assigning just 0.05 % of the experimental plasma power to the uniform plasma component, a model (in the filamentary regime) without vibrational excitation showed a very low steady state NH_3 density. We therefore identified that the micro-discharges, the uniform plasma component and vibrational excitation (which actually can take place during both the micro-discharges and the uniform plasma in between those micro-discharges) all play an important role in enhancing the NH_3 yield, through the dissociation rate of N_2.

Our results are all consistent with commonly made assumptions in literature, like the strong reduced electric field found in filamentary DBDs and the assumption that all plasma power is being deposited by filaments. However, slight sophistication of the latter assumption (i.e. 0.005 % to 0.4 % of the plasma power not assigned to the micro-discharges) has a major impact on the role of vibrational excitation in NH_3 synthesis in a DBD plasma. Indeed, our model reveals that, as soon as not all power is assigned to the micro-discharges, vibrational excitation is important for enhanced dissociation of N_2 in a (PB) DBD reactor, not only in the weaker uniform plasma but also during the strong micro-discharges.

Acknowledgments

This research was supported by the Excellence of Science FWO-FNRS project (FWO grant ID GoF9618n, EOS ID 30505023). The calculations were performed using the Turing HPC infrastructure at the CalcUA core facility of the Universiteit Antwerpen (UAntwerpen), a division of the Flemish Supercomputer Center VSC, funded by the Hercules Foundation, the Flemish Government (department EWI) and the UAntwerpen. The authors would

also like to thank Dr. Fatme Jardali for the discussions on plasma kinetic modelling and Dr. Jungmi Hong and Dr. Anthony B. Murphy for their aid in the calculation of the diffusion coefficients.

Appendix

A. Gas phase chemistry

A.1. Reaction list

Tables A.1 - A.4 list all rate coefficients of reactions between gas phase species in the model, except for detailed interactions between the various vibrationally excited states, which are described in Section A.2. In the tables, X,V and E indicate the ground state, vibrational levels and electronically excited states of a certain species (see Table 1 in the main text). The temperatures are given in Kelvin unless otherwise noted. Sometimes an effective ion temperature T_{ion} is used [64].

Table A.1 contains the electron impact reactions, and for most of them the rates are calculated from cross sections, indicated by $\sigma(\epsilon)$. The de-excitation rates are calculated using detailed balancing [54]. The rate coefficients (in cm^3s^{-1}) of G34, G35 and G36 are fits as a function of the electron temperature, adopted from [65].

$$k_{G34} = 7.51 \times 10^{-9} - 1.12 \times 10^{-9} T_e[\mathrm{eV}]^1 + 1.03 \times 10^{-10} T_e[\mathrm{eV}]^2 - 4.15 \times 10^{-12} T_e[\mathrm{eV}]^3 + 5.86 \times 10^{-14} T_e[\mathrm{eV}]^4 \quad \text{(A1)}$$

$$k_{G35} = k_{G36} = 0.5 \times (8.39 \times 10^{-9} + 3.02 \times 10^{-9} T_e[\mathrm{eV}]^1 - 3.80 \times 10^{-10} T_e[\mathrm{eV}]^2 + 1.31 \times 10^{-11} T_e[\mathrm{eV}]^3 + 2.42 \times 10^{-13} T_e[\mathrm{eV}]^4 - 2.30 \times 10^{-14} T_e[\mathrm{eV}]^5 + 3.55 \times 10^{-16} T_e[\mathrm{eV}]^6) \quad \text{(A2)}$$

Table A.2 lists the neutral-neutral collisions, Table A.3 presents the ion-neutral collisions, while Table A.4 shows the positive – negative ion collisions included in the model. The three-body collisions in Tables A.2 and A.4 are from [66], which are multiplied by $(1/380)$ (cf. ref [49]) to account for the reaction taking place at atmospheric pressure (760 Torr) [49], as opposed to low pressure (2 Torr) [66].

In Table A.4, the recombination and three-body recombination reactions all have the same rate coefficient.

Table A.1. Electron-impact reactions in the plasma kinetics model. X, V and E indicate the ground state, vibrational levels and electronically excited states of a certain species (see Table 1 in the main text). A reaction involving any type of gas phase species is indicated with M′. The temperatures are given in Kelvin unless otherwise noted.

	Excitation					
G1	$e + H_2(X,V)$	→	$H_2(E) + e$	$\sigma(\epsilon)$	[67]	1,2
G2	$e + N_2(X,V)$	→	$N_2(E) + e$	$\sigma(\epsilon)$	[67]	1,2
G3	$e + N$	→	$N(E) + e$	$\sigma(\epsilon)$	[67]	1
	De-excitation					
G4	$e + H_2(E)$	→	$H_2 + e$			3
G5	$e + N_2(E)$	→	$N_2 + e$			3
	Ionization					
G6	$e + N_2(X,V,E)$	→	$N_2^+ + e + e$	$\sigma(\epsilon)$	[68]	1,2
G7	$e + H_2(X,V)$	→	$H_2^+ + e + e$	$\sigma(\epsilon)$	[67]	1,2
G9	$e + N$	→	$N^+ + e + e$	$\sigma(\epsilon)$	[67]	1
G10	$e + H$	→	$H^+ + e + e$	$\sigma(\epsilon)$	[68]	1
G11	$e + NH$	→	$NH^+ + e + e$	$\sigma(\epsilon)$	[69]	1
G12	$e + NH_2$	→	$NH_2^+ + e + e$	$\sigma(\epsilon)$	[69]	1
G13	$e + NH_3$	→	$NH_3^+ + e + e$	$\sigma(\epsilon)$	[69]	1
	Dissociative Ionization					
G14	$e + N_2(X,V)$	→	$N^+ + N + e + e$	$\sigma(\epsilon)$	[70]	1
G15	$e + H_2$	→	$H + H^+ + e + e$	$\sigma(\epsilon)$	[71]	1
G16	$e + NH$	→	$H + N^+ + e + e$	$\sigma(\epsilon)$	[69]	1
G17	$e + NH_2$	→	$H + NH^+ + e + e$	$\sigma(\epsilon)$	[69]	1
G18	$e + NH_3$	→	$H + NH_2^+ + e + e$	$\sigma(\epsilon)$	[69]	1
	Dissociation					
G19	$e + H_2$	→	$H + H + e$	$\sigma(\epsilon)$	[71]	1
G20	$e + N_2(X,V,E)$	→	$N + N + e$	$\sigma(\epsilon)$	[67]	1,2
G21	$e + NH$	→	$N + H + e$	$5.0 \times 10^{-8}\, T_e[\mathrm{eV}]^{0.5} \exp(-8.6/T_e[\mathrm{eV}])$	[65]	
G22	$e + NH_2$	→	$N + H_2 + e$	$5.0 \times 10^{-8}\, T_e[\mathrm{eV}]^{0.5} \exp(-7.6/T_e[\mathrm{eV}])$	[65]	
G23	$e + NH_2$	→	$NH + H + e$	$5.0 \times 10^{-8}\, T_e[\mathrm{eV}]^{0.5} \exp(-7.6/T_e[\mathrm{eV}])$	[65]	
G24	$e + NH_3$	→	$NH_2 + H + e$	$5.0 \times 10^{-8}\, T_e[\mathrm{eV}]^{0.5} \exp(-4.4/T_e[\mathrm{eV}])$	[65]	
G25	$e + NH_3$	→	$NH + H_2 + e$	$5.0 \times 10^{-8}\, T_e[\mathrm{eV}]^{0.5} \exp(-5.5/T_e[\mathrm{eV}])$	[65]	
	(Dissociative) recombination					
G26	$e + N_2^+$	→	$N + N$	$0.50 \times 1.8 \times 10^{-7}(300/T_e)^{0.39}$	[64]	
G27	$e + N_2^+$	→	$N + N(^2D^0)$	$0.45 \times 1.8 \times 10^{-7}(300/T_e)^{0.39}$	[64]	
G28	$e + N_2^+$	→	$N + N(^2P^0)$	$0.05 \times 1.8 \times 10^{-7}(300/T_e)^{0.39}$	[64]	
G29	$e + N_3^+$	→	$N_2 + N$	$2.0 \times 10^{-7}(300/T_e)^{0.5}$	[64]	
G30	$e + N_3^+$	→	$N_2(A^3) + N$	$6.91 \times 10^{-8} T_e[\mathrm{eV}]^{-0.5}$	[72]	
G31	$e + N_3^+$	→	$N_2(B^3) + N$	$6.91 \times 10^{-8} T_e[\mathrm{eV}]^{-0.5}$	[72]	
G32	$e + N_4^+$	→	$N_2 + N_2$	$2.3 \times 10^{-6}(300/T_e)^{0.53}$	[64]	
G33	$e + N_4^+$	→	$N_2 + N + N$	$3.13 \times 10^{-7} T_e[\mathrm{eV}]^{-0.41}$	[72]	
G34	$e + H_2^+$	→	$H + H$	see Eq. A1	[65]	4
G35	$e + H_3^+$	→	$H + H + H$	see Eq. A2	[65]	4
G36	$e + H_3^+$	→	$H_2 + H$	see Eq. A2	[65]	4
G37	$e + NH^+$	→	$N + H$	$4.30 \times 10^{-8}(0.026/T_e[\mathrm{eV}])^{0.5}$	[65]	
G38	$e + NH_2^+$	→	$NH + H$	$1.02 \times 10^{-7}(0.026/T_e[\mathrm{eV}])^{0.4}$	[65]	
G39	$e + NH_2^+$	→	$N + H + H$	$1.98 \times 10^{-7}(0.026/T_e[\mathrm{eV}])^{0.4}$	[65]	
G40	$e + NH_3^+$	→	$NH + H + H$	$1.55 \times 10^{-7}(0.026/T_e[\mathrm{eV}])^{0.5}$	[65]	

G41	$e + NH_3^+$	→	$NH_2 + H$	$1.55 \times 10^{-7}(0.026/T_e[\mathrm{eV}])^{0.5}$	[65]	
G42	$e + NH_4^+$	→	$NH_3 + H$	$8.01 \times 10^{-7}(0.026/T_e[\mathrm{eV}])^{0.605}$	[65]	
G43	$e + NH_4^+$	→	$NH_2 + H + H$	$1.23 \times 10^{-7}(0.026/T_e[\mathrm{eV}])^{0.605}$	[65]	
G44	$e + N_2H^+$	→	$N_2 + H$	$7.1 \times 10^{-7}(0.026/T_e[\mathrm{eV}])^{0.72}$	[65]	
	Three-body recombination					
G45	$e + N^+ + e$	→	$N + e$	$7.0 \times 10^{-20}(300/T_e)^{4.5}$	[64]	
G46	$e + N^+ + M'$	→	$N + M'$	$6.0 \times 10^{-27}(300/T_e)^{1.5}$	[73]	
G47	$e + N_2^+ + e$	→	$N_2 + e$	$1.0 \times 10^{-19}(T_e/300)^{-4.5}$	[73]	
G48	$e + N_2^+ + M'$	→	$N_2 + M'$	$2.49 \times 10^{-29} T_e[\mathrm{eV}]^{-1.5}$	[72]	
	Attachment					
G49	$e + H_2(X,V)$	→	$H + H^-$	$\sigma(\epsilon)$	[74], [75]	[1,5]

[1] The rate coefficient is calculated from the electron impact cross section $\sigma(\epsilon)$ using BOLSIG+ [54]. The reference of the cross section is given.
[2] The cross section threshold energy is reduced when the reaction takes places from an excited state.
[3] The rate coefficients for de-excitation processes are calculated using detailed balancing [54].
[4] The rate coefficients are fits as a function of the electron temperature, given in Equation A1 and A2 [65].
[5] The cross section data is resolved for each individual vibrational state [74], [75].

Table A.2. Neutral-neutral collisions in the plasma kinetics model. X and V indicate the ground state and vibrational levels of a certain species (see Table 1 in the main text). A reaction involving any type of neutral gas phase species is indicated with M. Optionally, M is specified after a group of reactions. The temperatures are given in Kelvin.

	Neutral-neutral collisions					
G50	$N_2(X,V) + M$	→	$N + N + M$	$8.37 \times 10^{-4}(T_g/298)^{-3.50} \exp(-113710/T_g)$	[76]	[1]
G51	$N(^2D^0) + M$	→	$N + M$	2.4×10^{-14}	[77]	
G52	$N(^2P^0) + N$	→	$N(^2D^0) + N$	1.8×10^{-12}	[64]	
G53	$N(^2P^0) + N_2$	→	$N + N_2$	2.0×10^{-18}	[64]	
G54	$N_2(a'^1) + N$	→	$N_2 + N$	2.0×10^{-11}	[77]	
G55	$N_2(a'^1) + N_2$	→	$N_2 + N_2$	3.7×10^{-16}	[77]	
G56	$N_2(a'^1) + N_2$	→	$N_2(B^3) + N_2$	1.9×10^{-13}	[64]	
G57	$N_2(A^3) + N$	→	$N_2 + N(^2P^0)$	$4.0 \times 10^{-11}(300/T_g)^{0.667}$	[64]	
G58	$N_2(A^3) + N$	→	$N_2 + N$	2.0×10^{-12}	[64]	
G59	$N_2(A^3) + N_2$	→	$N_2 + N_2$	3.0×10^{-16}	[64]	
G60	$N_2(A^3) + N_2(A^3)$	→	$N_2 + N_2(A^3)$	2.0×10^{-12}	[77]	
G61	$N_2(A^3) + N_2(A^3)$	→	$N_2 + N_2(B^3)$	3.0×10^{-10}	[64]	
G62	$N_2(A^3) + N_2(A^3)$	→	$N_2 + N_2(C^3)$	1.5×10^{-10}	[64]	
G63	$N_2(B^3) + N_2$	→	$N_2 + N_2$	2.0×10^{-12}	[64]	
G64	$N_2(B^3) + N_2$	→	$N_2(A^3) + N_2$	3.0×10^{-11}	[64]	
G65	$N_2(C^3) + N_2$	→	$N_2(a'^1) + N_2$	1.0×10^{-11}	[64]	
G66	$N + NH$	→	$H + N_2$	5×10^{-11}	[66]	
G67	$H + NH$	→	$N + H_2$	$5.4 \times 10^{-11} \exp(-165/T_g)$	[66]	
G68	$NH + NH$	→	$H_2 + N_2$	$5 \times 10^{-14}(T_g/300)$	[66]	
G69	$NH + NH$	→	$N + NH_2$	$1.7 \times 10^{-12}(T_g/300)^{1.5}$	[66]	
G70	$NH + NH$	→	$N_2 + H + H$	8.5×10^{-11}	[66]	
G71	$H + NH_2$	→	$H_2 + NH$	$6.6 \times 10^{-11} \exp(-1840/T_g)$	[66]	
G72	$N + NH_2$	→	$N_2 + H + H$	1.2×10^{-10}	[66]	
G73	$N + NH_2$	→	$N_2 + H_2$	1.2×10^{-10}	[66]	

G74	$NH + NH_2$	→	$NH_3 + N$	1.66×10^{-12}	[66]	
G75	$H_2(V) + N$	→	$NH + H$	$4.0 \times 10^{-10}(T_g/300)^{0.5} \exp(-16600/T_g)$	[66]	[2]
G76	$H_2 + NH_2$	→	$NH_3 + H$	$5.4 \times 10^{-11} \exp(-6492/T_g)$	[66]	
G77	$H + NH_3$	→	$NH_2 + H_2$	$8.4 \times 10^{-14}(T_g/300)^{4.1} \exp(-4760/T_g)$	[66]	
G78	$N_2(A^3) + H$	→	$N_2 + H$	5×10^{-11}	[66]	
G79	$N_2(A^3) + H_2$	→	$N_2 + H + H$	$2 \times 10^{-10} \exp(-3500/T_g)$	[66]	
G80	$N_2(A^3) + NH_3$	→	$N_2 + NH_3$	1.6×10^{-10}	[66]	
G81	$N_2(B^3) + H_2$	→	$N_2(A^3) + H_2$	2.5×10^{-11}	[66]	
G82	$N_2(a'^1) + H$	→	$N_2 + H$	1.5×10^{-11}	[66]	
G83	$N_2(a'^1) + H_2$	→	$N_2 + H + H$	2.6×10^{-11}	[66]	
G84	$N + H_2(E)$	→	$H + NH$	$4.0 \times 10^{-10}(T_g/300)^{0.5}$	[49]	
G85	$N(^2D^0) + H_2$	→	$H + NH$	2.3×10^{-12}	[66]	
G86	$N(^2D^0) + NH_3$	→	$NH + NH_2$	1.1×10^{-10}	[66]	
G87	$N(^2P^0) + H_2$	→	$H + NH$	2.5×10^{-14}	[66]	
	Three-body collisions					
G88	$N + N + M$	→	$N_2 + M$	$1.38 \times^{-33} \exp(502.978/T_g)$	[78]	
G89	$N + N + N$	→	$N_2(A^3) + N$	1.0×10^{-32}	[64]	
G90	$N + N + N$	→	$N_2(B^3) + N$	1.4×10^{-32}	[64]	
G91	$N + N + N_2$	→	$N_2(A^3) + N_2$	1.7×10^{-33}	[64]	
G92	$N + N + N_2$	→	$N_2(B^3) + N_2$	2.4×10^{-33}	[64]	
G93	$N + N + H_2$	→	$N_2 + H_2$	$(1/380) \times 8.3 \times 10^{-34} \exp(500/T_g)$	[66]	[3]
G94	$H + H + N_2$	→	$H_2 + N_2$	$(1/380) \times 8.3 \times 10^{-33}(300/T_g)$	[66]	[3]
G95	$H + N + M$	→	$NH + M$	$(1/380) \times 1.0 \times 10^{-33}$	[66]	[3]
G96	$N + H_2 + M$	→	$NH_2 + M$	$(1/380) \times 1.0 \times 10^{-34}$	[66]	[3]
G97	$H + NH + M$	→	$NH_2 + M$	$(1/380) \times 1.0 \times 10^{-32}$	[66]	[3]
G98	$H + NH_2 + M$	→	$NH_3 + M$	$(1/380) \times 5.5 \times 10^{-30}$	[66]	[3]
G99	$NH + H_2 + M$	→	$NH_3 + M$	$(1/380) \times 2.5 \times 10^{-35}(T_g/300) \exp(1700/T_g)$	[66]	[3]
	$M = N_2(X,V), H_2(X,V)$					
G100	$N + N + H_2$	→	$N_2(A^3) + H_2$	$(1/380) \times 1.7 \times 10^{-33}$	[66]	[3]
G101	$N + N + H$	→	$N_2(A^3) + H$	$(1/380) \times 1.0 \times 10^{-32}$	[66]	[3]
G102	$N + N + H_2$	→	$N_2(B^3) + H_2$	$(1/380) \times 2.4 \times 10^{-33}$	[66]	[3]
G103	$N + N + H$	→	$N_2(B^3) + H$	$(1/380) \times 1.4 \times 10^{-32}$	[66]	[3]
G104	$H + H + H_2$	→	$H_2 + H_2$	$(1/380) \times 8.8 \times 10^{-33}(300/T_g)^{0.6}$	[66]	[3]
	Ionization processes					
G105	$N + N$	→	$N_2^+ + e$	$2.7 \times 10^{-11} \exp(-67400/T_g)$	[64]	
G106	$N_2(a'^1) + N_2(a'^1)$	→	$N_2^+ + N_2 + e$	5.0×10^{-13}	[77]	
G107	$N_2(a'^1) + N_2(a'^1)$	→	$N_4^+ + e$	1.0×10^{-11}	[64]	
G108	$N_2(a'^1) + N_2(a'^1)$	→	$N_4^+ + e$	4.0×10^{-12}	[64]	
G109	$N_2(A^3) + N_2(a'^1)$	→	$N_2^+ + N_2 + e$	1.0×10^{-12}	[77]	
	Radiative decay					
G110	$N_2(A^3)$	→	N_2	0.5	[64]	
G111	$N_2(B^3)$	→	$N_2(A^3)$	1.34×10^5	[64]	
G112	$N_2(a'^1)$	→	N_2	1.0×10^2	[64]	
G113	$N_2(C^3)$	→	$N_2(B^3)$	2.45×10^7	[64]	

[1] The rate coefficient is scaled according to the Fridmann-Macheret alpha-model [79] with $\alpha = 1$ [76].
[2] The reaction only occurs for the vibrational levels [66]. The reported rate coefficient is scaled according to the Fridmann-Macheret alpha-model [79] with $\alpha = 0.3$ [66].

[3] The rate coefficients of the three-body collisions are multiplied by (1⁄380) to account for the reaction taking place at atmospheric pressure [49], opposed to low pressure [66].

Table A.3. Ion-neutral collisions in the plasma kinetics model. X and V indicate the ground state and vibrational levels of a certain species (see Table 1 in the main text). The temperatures are given in Kelvin. An effective ion temperature T_{ion} is used [64].

	Ion-neutral collisions				
G114	$N^+ + H_2$	→	$NH^+ + H$	5.0×10^{-10}	[80]
G115	$N^+ + NH_3$	→	$NH_2^+ + NH$	$0.20 \times 2.35 \times 10^{-9}$	[80]
G116	$N^+ + NH_3$	→	$NH_3^+ + N$	$0.71 \times 2.35 \times 10^{-9}$	[80]
G117	$N^+ + NH_3$	→	$N_2H^+ + H_2$	$0.09 \times 2.35 \times 10^{-9}$	[80]
G118	$N_2^+ + N$	→	$N^+ + N_2$	$7.2 \times 10^{-13}(T_{ion}/300)$	[64]
G119	$N_2^+ + H_2$	→	$N_2H^+ + H$	2.00×10^{-9}	[65]
G120	$N_2^+ + N_2(A^3)$	→	$N_3^+ + N$	3.0×10^{-10}	[81]
G121	$N_2^+ + NH_3$	→	$NH_3^+ + N_2$	1.95×10^{-9}	[65]
G122	$N_3^+ + N$	→	$N_2^+ + N_2$	6.6×10^{-11}	[64]
G123	$N_4^+ + N$	→	$N^+ + N_2 + N_2$	1.0×10^{-11}	[64]
G124	$N_4^+ + N_2$	→	$N_2^+ + N_2 + N_2$	$2.1 \times 10^{-16} \exp(T_{ion}/121)$	[64]
G125	$H^+ + NH_3$	→	$NH_3^+ + H$	5.20×10^{-9}	[80]
G126	$H_2^+ + H$	→	$H^+ + H_2$	6.4×10^{-10}	[65]
G127	$H_2^+ + H_2$	→	$H_3^+ + H$	2.0×10^{-9}	[65]
G128	$H_2^+ + N_2$	→	$N_2H^+ + H$	2.00×10^{-9}	[80]
G129	$H_2^+ + NH_3$	→	$NH_3^+ + H_2$	5.70×10^{-9}	[80]
G130	$NH^+ + H_2$	→	$H_3^+ + N$	$0.15 \times 1.23 \times 10^{-9}$	[80]
G131	$NH^+ + H_2$	→	$NH_2^+ + H$	$0.85 \times 1.23 \times 10^{-9}$	[80]
G132	$NH^+ + NH_3$	→	$NH_3^+ + NH$	$0.75 \times 2.40 \times 10^{-9}$	[80]
G133	$NH^+ + NH_3$	→	$NH_4^+ + N$	$0.25 \times 2.40 \times 10^{-9}$	[80]
G134	$NH^+ + N_2$	→	$N_2H^+ + N$	6.50×10^{-10}	[80]
G135	$NH_2^+ + H_2$	→	$NH_3^+ + H$	1.95×10^{-10}	[80]
G136	$NH_2^+ + NH_3$	→	$NH_3^+ + NH_2$	$0.5 \times 2.30 \times 10^{-9}$	[80]
G137	$NH_2^+ + NH_3$	→	$NH_4^+ + NH$	$0.5 \times 2.30 \times 10^{-9}$	[80]
G138	$NH_3^+ + NH_3$	→	$NH_4^+ + NH_2$	2.10×10^{-9}	[80]
G139	$N_2H^+ + NH_3$	→	$NH_4^+ + N_2$	2.3×10^{-9}	[80]
	Ion-neutral three-body collisions				
G140	$N_2^+ + N + N_2$	→	$N_3^+ + N_2$	$9.0 \times 10^{-30} \exp(400/T_{ion})$	[64]
G141	$N^+ + N_2 + N_2(X,V)$	→	$N_3^+ + N_2$	$1.7 \times 10^{-29}(300/T_{ion})^{2.1}$	[64]
G142	$N_2^+ + N_2 + N_2(X,V)$	→	$N_4^+ + N_2$	$5.2 \times 10^{-29}(300/T_{ion})^{2.2}$	[64]
G143	$N^+ + N + N_2$	→	$N_2^+ + N_2$	1.0×10^{-29}	[64]

Table A.4. Positive - negative ion recombination collisions in the plasma kinetics model. X and V indicates the ground state and vibrational levels of a certain species (see Table 1 in the main text). The third colliding particle is indicated with M and specified after the group of reactions. The temperatures are given in Kelvin. Within each type of reaction, all reactions are assumed to have the same rate coefficient.

	H^- recombination	$2.0 \times 10^{-7}(300/T_g)$	[66]
G144	$H^- + H_2^+ \rightarrow H + H + H$		
G145	$H^- + H_3^+ \rightarrow H_2 + H + H$		
G146	$H^- + N_2^+ \rightarrow N_2 + H$		
G147	$H^- + N_4^+ \rightarrow N_2 + N_2 + H$		
G158	$H^- + N_2H^+ \rightarrow H_2 + N_2$		
	H^- three-body recombination	$(1/380) \times 2 \times 10^{-25}(300/T_g)^{2.5}$	[66] [1]
G149	$H^- + H_2^+ + M \rightarrow H_2 + H + N_2$		
G150	$H^- + H_3^+ + M \rightarrow H_2 + H_2 + M$		
G151	$H^- + N_2^+ + M \rightarrow N_2 + H + M$		
G152	$H^- + N_4^+ + M \rightarrow N_2 + N_2 + H + M$		
G153	$H^- + N_2H^+ + M \rightarrow H_2 + N_2 + M$		
	$M = N_2(X,V), H_2(X,V), N, H$		

[1] The rate coefficients of the three-body collisions are multiplied by (1⁄380) to account for the reaction taking place at atmospheric pressure [49], as opposed to low pressure [66].

A.2. Vibrational kinetics

Tables A.1 - A.4 indicated some reactions (G1, G2, G6, G7, G14, G20, G49, G95-99, G141, G142 and G149-153) which are also considered for the vibrational levels. For reactions G1, G2, G6, G7 and G20, the corresponding cross section threshold energy is scaled according to the vibrational energy, while G14 assumes the same cross section. Reaction G49, i.e. dissociative attachment of H_2, uses a vibrationally resolved cross section set [74], [75]. The ground state rate coefficient expressions are used for the vibrational states in reactions G95-99, G141, G142 and G149-153. Furthermore, Table A.2 includes $H_2(V) + N \rightarrow NH + H$ (G75), which only occurs for the vibrational levels [66]. The reported rate coefficient, in Table A.2, is scaled according to the Fridmann-Macheret alpha-model [79] with $\alpha = 0.3$ [66]. The same principle is applied to G50 (Table A.2) with $\alpha = 1$ [76].

The remaining processes involving the vibrational levels are listed here, with the rate coefficient expressions, given according to their respective references.

We include excitation and de-excitation of both $N_2(V)$ and $H_2(V)$ through the vibrationally resolved resonant vibrational excitation cross sections from the Phys4Entry database [57], [61], [62], [82].

$$e + N_2(v) \leftrightarrow N_2(v' > v) + e, \qquad v = 1 \ldots 24 \tag{A3}$$

$$e + H_2(v) \leftrightarrow H_2(v' > v) + e, \qquad v = 1 \dots 3 \tag{A4}$$

Similarly, for $H_2(V)$ we included the vibrationally resolved dissociative attachment, as already indicated in Table A.1 (G49) [74], [75].

Finally, we included various vibrational-translational (VT) and vibrational-vibrational (VV) relaxation processes, which will be listed here. For the actual calculations or rate coefficient expressions we refer to the respective publications. N_2-N VT relaxation is included using the rate coefficient calculated by Esposito et al. [59]

$$N_2(v) + N \leftrightarrow N_2(v' < v) + N, \qquad v = 1 \dots 24 \tag{A5}$$

which includes all the individual single and multi-quantum jumps.

The N_2-N_2 VT relaxation

$$N_2(v) + N_2 \leftrightarrow N_2(v - 1) + N_2, \qquad v = 1 \dots 24 \tag{A6}$$

and the N_2-N_2 VV relaxation

$$N_2(v + 1) + N_2(w) \leftrightarrow N_2(v) + N_2(w + 1), \qquad v = 1 \dots 24, \qquad w < v \tag{A7}$$

are adopted from Adamovich et al. [58]. They are fitted, as a function of temperature, to an appropriate rate coefficient expression.

The H_2-H_2 VT relaxation

$$H_2(v) + H_2 \leftrightarrow H_2(v - 1) + H_2, \qquad v = 1 \dots 3 \tag{A8}$$

and the H_2-H_2 VV relaxation

$$H_2(v + 1) + H_2(w) \leftrightarrow H_2(v) + H_2(w + 1), \qquad v = 1 \dots 3, \qquad w < v \tag{A9}$$

are implemented using the SSH (Schwartz, Slawsky and Herzfeld) theory [64], [83]. The SSH theory rates are also fitted to an appropriate temperature dependent expression. The SSH theory is also used for H_2-H VT relaxation, adopted from Gordiets et al. [66]

$$H_2(v) + H \leftrightarrow H_2(v-1) + H, \qquad v = 1 \dots 3 \tag{A10}$$

$$H_2(v) + H \leftrightarrow H_2 + H, \qquad v = 1 \dots 3 \tag{A11}$$

where only the individual one-quantum transitions are included. Multi-quantum processes use a rate coefficient that represents the effective sum of all the transitions [66]. The relaxations between nitrogen and hydrogen are also after Gordiets et al., using the SSH theory. N_2-H_2 VT, N_2-H VT (with similar treatment of one- and multi-quantum jumps to H_2-H VT relaxation, i.e. processes A10 and A11) and H_2-N_2 VV relaxation, respectively, are included.

$$N_2(v) + H_2 \leftrightarrow N_2(v-1) + H_2, \qquad v = 1 \dots 8 \tag{A12}$$

$$N_2(v) + H \leftrightarrow N_2(v-1) + H, \qquad v = 1 \dots 8 \tag{A13}$$

$$N_2(v) + H \leftrightarrow N_2 + H, \qquad v = 1 \dots 8 \tag{A14}$$

$$H_2(v) + N_2(w-1) \leftrightarrow H_2(v-1) + N_2(w), \qquad v = 1 \dots 3, \qquad w = 1 \dots 8 \tag{A15}$$

H_2-N_2 VT relaxation is insignificant compared to the other processes, while two-quantum N_2-H_2 VV relaxations are included [66].

$$N_2(v) + H_2(w-1) \leftrightarrow N_2(v-2) + H_2(w), \qquad v = 2 \dots 8, \qquad w = 1 \dots 3 \tag{A16}$$

B. Surface kinetics

We adopted the surface kinetics module from Hong et al. [49] and Shah et al. [52] and we adopted their sticking probability values for metal surfaces. The rate coefficients are calculated using Chantry's formula [65], [84].

Table B.1 lists the reactions included in the surface model, together with the relevant parameters to calculate their rate coefficients. In total, wall relaxation (wall), direct adsorption (ads), Eley-Rideal (ER), Langmuir-Hinshelwood (LH) and dissociative adsorption (dads) are taken into account.

Table B.1. Surface reactions included in the model, together with the sticking probabilities γ or relevant energies E, corresponding to metal surfaces, and the references from where those values are adopted. X and V indicate the ground state and vibrational levels of a certain species (see Table 1 in the main text).

#					Ref.
	Wall relaxation				
S1	$N_2(A^3)$	$\rightarrow$	N_2	$\gamma_{wall} = 1 \times 10^{-3}$	[66]
S2	$N_2(A^1)$	$\rightarrow$	$N_2(B^3)$	$\gamma_{wall} = 1 \times 10^{-3}$	[66]
S3	$H_2(E)$	$\rightarrow$	H_2	$\gamma_{wall} = 1 \times 10^{-3}$	[66]
S4	$N_2(V)$	$\rightarrow$	$N_2(V-1)$	$\gamma_{wall} = 1 \times 10^{-4}$	[66]
S5	$H_2(V)$	$\rightarrow$	$H_2(V-1)$	$\gamma_{wall} = 4.5 \times 10^{-4}$	[66]
	Direct adsorption				
S6	$N(X,E) + surf$	$\rightarrow$	$N(s)$	$\gamma_{ads} = 1$	[65]
S7	$H + surf$	$\rightarrow$	$H(s)$	$\gamma_{ads} = 1$	[65]
S8	$NH + surf$	$\rightarrow$	$NH(s)$	$\gamma_{ads} = 1$	[65]
S9	$NH_2 + surf$	$\rightarrow$	$NH_2(s)$	$\gamma_{ads} = 1$	[65]
	Eley-Rideal				
S10	$N(X,E) + N(s)$	$\rightarrow$	$N_2 + surf$	$\gamma_{ER} = 6 \times 10^{-3}$	[65]
S11	$H + H(s)$	$\rightarrow$	$H_2 + surf$	$\gamma_{ER} = 1.5 \times 10^{-3}$	[65]
S12	$N(X,E) + H(s)$	$\rightarrow$	$NH(s)$	$\gamma_{ER} = 1 \times 10^{-2}$	[65]
S13	$NH + H(s)$	$\rightarrow$	$NH_2(s)$	$\gamma_{ER} = 1 \times 10^{-2}$	[65]
S14	$H + N(s)$	$\rightarrow$	$NH(s)$	$\gamma_{ER} = 8 \times 10^{-3}$	[65]
S15	$H + NH(s)$	$\rightarrow$	$NH_2(s)$	$\gamma_{ER} = 8 \times 10^{-3}$	[65]
	Eley-Rideal: NH_3 formation				
S17	$NH_2 + H(s)$	$\rightarrow$	$NH_3 + surf$	$\gamma_{ER} = 1 \times 10^{-2}$	[65]
S18	$H + NH_2(s)$	$\rightarrow$	$NH_3 + surf$	$\gamma_{ER} = 8 \times 10^{-3}$	[65]
S19	$H_2(X,V) + NH(s)$	$\rightarrow$	$NH_3 + surf$	$\gamma_{ER} = 8 \times 10^{-4}$	[65]
	Langmuir-Hinshelwood				
S20	$N(s) + H(s)$	$\rightarrow$	$NH(s) + surf$	$E_a = 1.099$ eV $E_d = 0.2$ eV	[49]
S21	$NH(s) + H(s)$	$\rightarrow$	$NH_2(s) + surf$	$E_a = 0.3$ eV $E_d = 0.2$ eV	[65]
S22	$NH_2(s) + H(s)$	$\rightarrow$	$NH_3 + surf + surf$	$E_a = 0.2$ eV $E_d = 0.2$ eV	[65]
	Dissociative adsorption				
S23	$N_2(X,V) + surf + surf$	$\rightarrow$	$N(s) + N(s)$	$\bar{\gamma}_{dads,N_2}(X,V)$	[85], [86]
S24	$N_2(E) + surf + surf$	$\rightarrow$	$N(s) + N(s)$	$\gamma_{dads} = 1 \times 10^{-1}$	[49]
S25	$H_2 + surf + surf$	$\rightarrow$	$H(s) + H(s)$	$\gamma_{dads} = 1 \times 10^{-3}$	[49]

S26	$H_2(V = 1) + surf + surf$	$\rightarrow$	$H(s) + H(s)$	$\gamma_{dads} = 1 \times 10^{-2}$	[49]
S27	$H_2(V = 2) + surf + surf$	$\rightarrow$	$H(s) + H(s)$	$\gamma_{dads} = 5 \times 10^{-2}$	[49]
S28	$H_2(V \geq 3) + surf + surf$	$\rightarrow$	$H(s) + H(s)$	$\gamma_{dads} = 1 \times 10^{-1}$	[49]
S29	$H_2(E) + surf + surf$	$\rightarrow$	$H(s) + H(s)$	$\gamma_{dads} = 1 \times 10^{-2}$	[49]

The rate coefficients are calculated with equations B1 - B5, for the various processes. In those equations, γ is the sticking probability, $\bar{v} = \sqrt{8k_BT/\pi m}$ is the average velocity of the gas phase species in the reaction, (V/A) is the volume to surface area ratio of the reactor, Λ is the diffusion length, D is the diffusion coefficient, $\nu \approx 10^{-13}$ s^{-1} is the surface diffusional jump frequency [87], E_d is the diffusion energy barrier and E_a is the activation energy. We assume the wall temperature T_{wall} equal to the gas temperature T_g and k_B is the Boltzmann constant. The total surface site density S_T in cm^{-2} is used to convert the rate coefficients from s^{-1} to cm^2s^{-1} or to cm^4s^{-1} where appropriate. Subsequently, this rate is multiplied by (V/A) to convert the rate coefficients to cm^3s^{-1} and cm^6s^{-1}, respectively – as already included in the equations. The volume to surface area ratio of the reactor (V/A) and the total surface site density (S_T) are adopted from [52].

$$k_{wall} = \left[\frac{\Lambda^2}{D} + \left(\frac{V}{A}\right)\frac{2(2-\gamma_{wall})}{\bar{v}\gamma_{wall}}\right]^{-1} \tag{B1}$$

$$k_{ads} = \left[\frac{\Lambda^2}{D} + \left(\frac{V}{A}\right)\frac{2(2-\gamma_{ads})}{\bar{v}\gamma_{ads}}\right]^{-1} \times S_T^{-1} \times \left(\frac{V}{A}\right) \tag{B2}$$

$$k_{ER} = \left[\frac{\Lambda^2}{D} + \left(\frac{V}{A}\right)\frac{2(2-\gamma_{ER})}{\bar{v}\gamma_{ER}}\right]^{-1} \times S_T^{-1} \times \left(\frac{V}{A}\right) \tag{B3}$$

$$k_{LH} = \frac{\nu}{4} exp\left(-\frac{E_a + E_d}{k_B T_{wall}}\right) \times S_T^{-1} \times \left(\frac{V}{A}\right) \tag{B4}$$

$$k_{dad} = \left[\frac{\Lambda^2}{D} + \left(\frac{V}{A}\right)\frac{2(2-\gamma_{dad})}{\bar{v}\gamma_{dad}}\right]^{-1} \times S_T^{-2} \times \left(\frac{V}{A}\right)^2 \tag{B5}$$

The diffusion length is given by $\Lambda = R/2.405$, with R the radius of the reactor. For a packed bed reactor we assume a reduced diffusion length $\Lambda = 0.2 \times R/2.405$ [52].

The diffusion coefficients for N, H, N_2, H_2, NH and NH_2 in both N_2 and H_2 were calculated from collision integrals [88], adopted by Murphy [89]. In addition, the NH_2-NH_2 interaction was calculated in a similar fashion as the NH-NH interaction, as described in [89] – using the force constants of NH and H instead of N and H. For any missing interaction, a combination rule was assumed [90]. In Table B.2 the adopted diffusion coefficients are listed, evaluated at 400 K. The actual diffusion coefficient for the mixing ratio of N_2 and H_2 is calculated using Blanc's law [91].

Table B.2. Diffusion coefficients in N_2 and H_2 at 400 K, as used in the model.

	D_{ij} [$m^2 s^{-1}$]	
$i =$	$j = N_2$	$j = H_2$
N	6.910×10^{-5}	2.234×10^{-4}
H	2.005×10^{-4}	3.650×10^{-4}
N_2	3.470×10^{-5}	1.700×10^{-4}
H_2	1.262×10^{-4}	2.497×10^{-4}
NH	5.848×10^{-5}	1.871×10^{-4}
NH_2	5.260×10^{-5}	1.681×10^{-4}

For the dissociative adsorption of N_2 from the ground state and vibrationally excited states (S23), the sticking probability is given by $\gamma_{dads} = \bar{\gamma}_{dads,N_2}(\mathrm{V})$, which is the average sticking probability, with $\mathrm{V} = 0 \ldots 10$ ($\mathrm{V} = 0$ corresponds to X, i.e. the ground state in process S23 (Table B.1)). We calculated this average value with

$$\bar{\gamma}_{dads}(\mathrm{V}) = \frac{\int P(E_z) \times \gamma_{dads}(E_z, \mathrm{V})\, dE_z}{\int P(E_z)\, dE_z} \tag{B6}$$

where E_z is the kinetic energy of a species hitting the surface, perpendicular to the surface itself and $P(E_z)$ is the probability distribution function, proportional to those species hitting the surface, given by [85], [86]

$$P(E_z) = \frac{1}{\sqrt{2\pi M k_B T_g}} \times \sqrt{\frac{E_z}{k_B T_g}} \times \exp\left(-\frac{E_z}{k_B T_g}\right) \tag{B7}$$

where M is the mass of N_2. The sticking probability, $\gamma_{dads}(E_z, \mathrm{V})$, as a function of the kinetic energy and vibrational level of the incoming species, is given by [85], [86]

$$\log_{10}[\gamma_{dads}(E_z, \mathrm{V})] = a_{\mathrm{V}} + b_{\mathrm{V}} \times [1 - \exp(-c_{\mathrm{V}} E_z)] + [1 - \exp(-d_{\mathrm{V}} E_z)] \tag{B8}$$

where a_V, b_V, c_V and d_V are fit parameters, given in Table 1 of [86]. We assume the parameters of $V = 10$ for all vibrational levels higher than 10.

C. Power density description in the model

C.1. Derivation of the time-dependent power density function

As described in Section 2.3 in the main text, we have defined the power density as a function of time. The individual micro-discharges are triangular power density pulses with a duration (i.e. width or life time), τ_{MD}. Initially, we take the actual pulse period $T_P = T_D/2N_{MD}$, i.e. the discharge period over the number of micro-discharges per period ($2N_{MD}$). This considers all the micro-discharges taking place anywhere in the reactor.

In Section 2.3 we explained that individual molecules cannot be exposed to all the micro-discharges taking place throughout the whole reactor during a certain residence time τ_{res}. This introduces a fraction of micro-discharges to which the molecules are exposed: $\eta_{MD} = vT_D/L_R = QT_D/V_R = T_D/\tau_{res}$, where v and Q are the gas velocity and flow rate, respectively, and L_R and V_R are the reactor length and volume, respectively. Because of this concept, we actually use a modified pulse period $T_P^\eta = T_P/\eta_{MD}$, which reduces to $T_P^\eta = \tau_{res}/2N_{MD}$. We centre the actual pulse around $t_0^\eta = T_P^\eta/2$. All definitions related to the periodic micro-discharge pulses are depicted on the x-axis of Figure C.1.

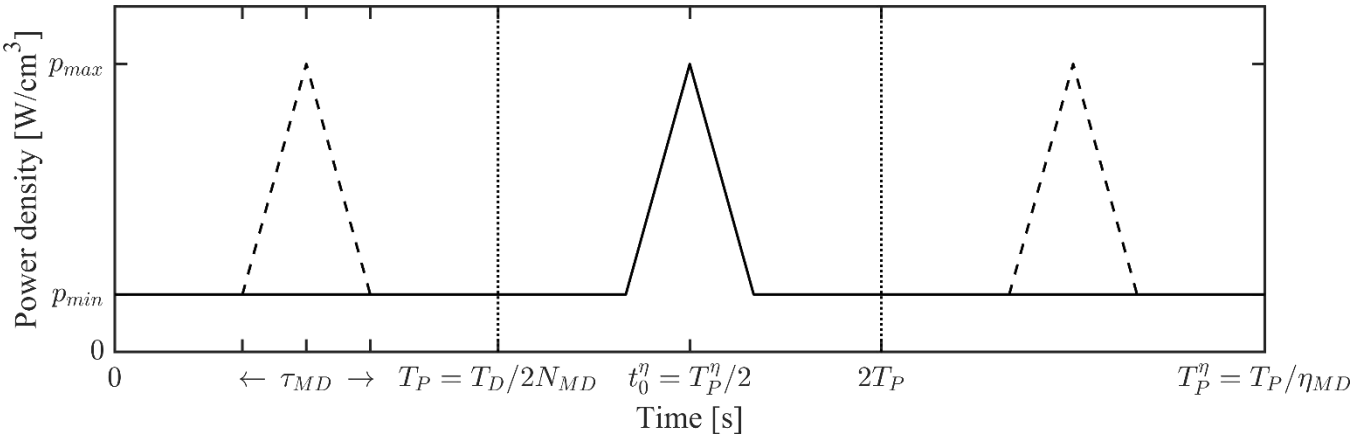

Figure C.1. Definition of the power density pulse in time (Eq. C1), with p_{max} and p_{min} being the maximum power density in the pulse and the power density in between the pulses, respectively, τ_{MD} the micro-discharge life time, N_{MD} the number of micro-discharges per half cycle, η_{MD} the fraction of micro-discharges to which molecules are exposed (depicted here as $\eta_{MD} = 1/3$), T_D the discharge period, T_P the pulse period based on all micro-discharges that occur throughout the whole reactor and t_0^η the pulse location and T_P^η the pulse period corresponding to the micro-discharges to which individual molecules are exposed to (on average).

We define the average power density $\bar{p} = P/V$, in which P is the total plasma power (i.e. as determined from an experimental setup) and V is the chosen discharge volume in which the total plasma power is deposited. Both the total plasma power and the chosen discharge volume are constants in our model description. In the periodic power density function, $p(t)$, we define the maximum and minimum power density values, p_{max} and p_{min}, as depicted in Figure C.1. The (piecewise) power density function can be given by

$$p^{\eta}\left(t_{mod}^{\eta}\right) = (p_{max} - p_{min}) \times \frac{2}{\tau_{MD}} \times \max\left[\left(\frac{\tau_{MD}}{2} - \left|t_{mod}^{\eta} - t_0\right|\right), 0\right] + p_{min} \tag{C1}$$

where the periodicity is achieved by using $t_{mod}^{\eta} = t \bmod T_P^{\eta}$. If we consider all the micro-discharges that take place in the reactor (i.e. dropping the superscript η), we can rewrite the average power density $\bar{p} = P/V$, during a single pulse period as

$$\begin{aligned} \bar{p} = \frac{P}{V} &= \frac{1}{T_P}\int_0^{T_P} p(t)\, dt \\ &= (p_{max} - p_{min})\frac{\tau_{MD}}{2T_P} + p_{min} \\ &= \left[(1-\gamma)\frac{\tau_{MD}}{2T_P} + \gamma\right] p_{max} \end{aligned} \tag{C2}$$

where we define $p_{min} = \gamma p_{max}$ by introducing the power density distribution factor $\gamma \in [0,1]$. The first term in the summation in Equation C2 represents the micro-discharges and the second term represents a uniform plasma component that is always present. The maximum power density follows from Equation C2 as

$$p_{max} = \frac{P/V}{(1-\gamma)\frac{\tau_{MD}}{2T_P} + \gamma} \tag{C3}$$

The total plasma power P can then also be considered as the sum of the power deposited into the plasma by the micro-discharges, P_{MD}, and by the uniform plasma, P_U, i.e.

$$P = P_{MD} + P_U \tag{C4}$$

Because the power attributed to the micro-discharges is deposited locally, instead of uniformly throughout the reactor, we have to apply the fraction of micro-discharges η_{MD}, if we consider individual molecules flowing through the reactor. The total power P^{η} deposited into the molecules is then

$$P^{\eta} = P_{MD}^{\eta} + P_U = \eta_{MD} P_{MD} + P_U \tag{C5}$$

Thus, in principle, our model will consider the total power deposited into the molecules, P^{η}, instead of the total plasma power, P, i.e. a lower total power.

By taking the average of $p^{\eta}(t)$ (Eq. C1), analogous to Equation C2, and separately integrating the first and second term in the resulting summation (cf. Eq. C2) over the discharge volume, we receive relationships between the total power components and the power density distribution factor as follows

$$P_{MD}^{\eta} = \left[\frac{(1-\gamma)\frac{\tau_{MD}}{2T_P^{\eta}}}{(1-\gamma)\frac{\tau_{MD}}{2T_P} + \gamma} \right] P \tag{C6}$$

$$P_U = \left[\frac{\gamma}{(1-\gamma)\frac{\tau_{MD}}{2T_P} + \gamma} \right] P \tag{C7}$$

Those relationships can be used to determine the fraction of power attributed to the micro-discharges and the uniform plasma.

As a final remark, we would like to point out that in this paper we chose to study the power density distribution factor γ instead of a direct distribution of the power, because this allows us to confine ourselves to a choice of the total plasma power P and a single choice of the discharge volume V. Furthermore, we believe that making such an actual distinction in experiments requires further sophistication of the calculations typically performed on the current, voltage and charge characteristics of a DBD.

C.2. Choice of discharge volume

In order to calculate the maximum and minimum power densities in the pulse, the average power density is required and this requires a choice of the relevant discharge volume V. We assume the latter to be equal to: $V = 2N_{MD} \cdot 10^{-5}$ cm^3. The latter value (10^{-5} cm^3) was chosen based on calculations of single filament volumes ($1.6 \cdot 10^{-5}$ cm^3 in [60]) and approximated volumes of single voids in a DBD reactor packed with spherical beads, because various kinds of local micro-discharges are known to occur in between the packing material [33]. Using the void sphere radii calculated in [92] and the bead sizes studied in [17], values for single void volumes in the order of 10^{-3} to 10^{-7} cm^3 were retrieved.

Thus we model the full plasma reactor, in the sense that we consider the full residence time of the gas flowing through the reactor. However, in this model definition, the reactor volume is only used in converting the rate coefficients of the surface kinetic processes (see Appendix B). In relation to the actual plasma power, we consider a specific volume in which this power is deposited, i.e. the discharge volume, which represents all the micro-discharges during a single discharge period, because the experimentally measured power is measured during a single discharge period (typically the average is taken over several full periods).

C.3. Describing packed bed DBDs

One motivation for the development of this new model approach (Section 2.3 and Appendix C), is to be able to describe a PB reactor. Being able to systematically describe an unpacked and packed reactor, and distinguish them from each other, in 0D plasma chemistry modelling is of high interest. As a summary, accounting for PB DBDs in our model is achieved in multiple ways. First, through the introduction of the fraction of micro-discharges η_{MD}, which uses the gas velocity, the flow rate or residence time. In PB reactors, the gas volume in the reactor may be different for different packing configurations (and they are also smaller than for unpacked reactors), thus flow rates are different for equal residence times, or vice versa, the residence time is different for equal flow rates [34]. Those quantities are systematically taken into account. The use of η_{MD} also returns a number of micro-discharges in the model, which is found to correspond directly to the actual (experimentally) measured number of micro-discharges. The number of micro-discharges has also been shown to change upon introducing a packing material under the same experimental conditions [34]. Second, in calculating the discharge volume (for the micro-

discharges), the size of a single void between the spheres can be used, meaning that the actual bead size is taken into account [92]. In calculating the (V/A) ratio (for use in the surface kinetics in 0D plasma kinetic solvers, in units of cm^{-3} instead of cm^{-2} – see Appendix B), the surface area A should also depend on the actual packing [49], [52]. Finally, the distinction between a filamentary and uniform plasma component (Eq. C5) has a clear physical meaning. In this work we differentiate between the two through a power density distribution factor γ. 2D modelling has shown that, depending on the dielectric constant of the packing material, the electric field is enhanced near the surface of the beads, giving rise to mainly local filamentary discharges (at low values of the dielectric constant) or mainly surface discharges (at high values of the dielectric constant) or a combination of both (at intermediate values) [33]. While the predominance of local filamentary discharges corresponds to small values of γ, higher values of γ would refer to the presence of surface discharges.

References

[1] C. J. Dawson and J. Hilton, "Fertiliser availability in a resource-limited world: Production and recycling of nitrogen and phosphorus," *Food Policy*, vol. 36, pp. S14–S22, 2011.

[2] J. Brightling, "Ammonia and the Fertiliser Industry: The Development of Ammonia at Billingham," *Johnson Matthey Technol. Rev.*, no. 1, pp. 32–47, 2018.

[3] Y. Bicer, I. Dincer, C. Zam, G. Vezina, and F. Raso, "Comparative life cycle assessment of various ammonia production methods," *J. Clean. Prod.*, vol. 135, pp. 1379–1395, 2016.

[4] U. Kogelschatz, B. Eliasson, and W. Egli, "From ozone generators to flat television screens: history and future potential of dielectric-barrier discharges," *Pure Appl. Chem.*, vol. 71, no. 10, pp. 1819–1828, 1999.

[5] A. Bogaerts and E. C. Neyts, "Plasma Technology: An Emerging Technology for Energy Storage," *ACS Energy Lett.*, vol. 3, no. 4, pp. 1013–1027, Apr. 2018.

[6] P. Peng *et al.*, "A review on the non-thermal plasma-assisted ammonia synthesis technologies," *J. Clean. Prod.*, vol. 177, pp. 597–609, 2018.

[7] M. L. Carreon, "Plasma catalytic ammonia synthesis: state of the art and future directions," *J. Phys. D. Appl. Phys.*, vol. 52, p. 483001, 2019.

[8] M. Bai, X. Bai, Z. Zhang, and M. Bai, "Synthesis of Ammonia in a Strong Electric Field Discharge at Ambient Pressure," Plasma Chem. Plasma Process., vol. 20, no. 4, pp. 511–520, 2000.

[9] M. Bai, Z. Zhang, X. Bai, M. Bai, and W. Ning, "Plasma Synthesis of Ammonia With a Microgap Dielectric Barrier Discharge at Ambient Pressure," IEEE Trans. Plasma Sci., vol. 31, no. 6, pp. 1285–1291, 2003.

[10] T. Mizushima, K. Matsumoto, J. I. Sugoh, H. Ohkita, and N. Kakuta, "Tubular membrane-like catalyst for reactor with dielectric-barrier- discharge plasma and its performance in ammonia synthesis," Appl. Catal. A Gen., vol. 265, no. 1, pp. 53–59, 2004.

[11] T. Mizushima, K. Matsumoto, H. Ohkita, and N. Kakuta, "Catalytic effects of metal-loaded membrane-like alumina tubes on ammonia synthesis in atmospheric pressure plasma by dielectric barrier discharge," Plasma

Chem. Plasma Process., vol. 27, no. 1, pp. 1–11, 2007.

[12] A. Gómez-Ramírez, J. Cotrino, R. M. Lambert, and A. R. González-Elipe, "Efficient synthesis of ammonia from N_2 and H_2 alone in a ferroelectric packed-bed DBD reactor," Plasma Sources Sci. Technol., vol. 24, p. 065011, 2015.

[13] A. Gómez-ramírez and R. M. Lambert, "About the enhancement of chemical yield during the atmospheric plasma synthesis of ammonia in a ferroelectric packed bed reactor," Plasma Process. Polym., vol. 2016, no. August, pp. 1–8, 2016.

[14] P. Barboun, P. Mehta, F. A. Herrera, D. B. Go, W. F. Schneider, and J. C. Hicks, "Distinguishing Plasma Contributions to Catalyst Performance in Plasma-Assisted Ammonia Synthesis," ACS Sustain. Chem. Eng., vol. 7, pp. 8621–8630, 2019.

[15] P. Peng, Y. Li, Y. Cheng, and S. Deng, "Atmospheric Pressure Ammonia Synthesis Using Non-thermal Plasma Assisted Catalysis," Plasma Chem. Plasma Process., vol. 36, no. 5, pp. 1201–1210, 2016.

[16] G. Akay and K. Zhang, "Process intensification in ammonia synthesis using novel coassembled supported microporous catalysts promoted by nonthermal plasma," Ind. Eng. Chem. Res., vol. 56, no. 2, pp. 457–468, 2017.

[17] K. Van Laer and A. Bogaerts, "How bead size and dielectric constant affect the plasma behaviour in a packed bed plasma reactor: a modelling study," *Plasma Sources Sci. Technol.*, vol. 26, no. 8, p. 85007, 2017.

[18] N. Y. Babaeva and M. J. Kushner, "Effect of inhomogeneities on streamer propagation: I. Intersection with isolated bubbles and particles," *Plasma Sources Sci. Technol.*, vol. 18, p. 035009, 2009.

[19] N. Y. Babaeva and M. J. Kushner, "Effect of inhomogeneities on streamer propagation: II. Streamer dynamics in high pressure humid air with bubbles," *Plasma Sources Sci. Technol.*, vol. 18, p. 035010, 2009.

[20] N. Y. Babaeva, A. N. Bhoj, and M. J. Kushner, "Streamer dynamics in gases containing dust particles," Plasma Sources Sci. Technol., vol. 15, pp. 591–602, 2006.

[21] R. Dorai and M. J. Kushner, "A model for plasma modification of polypropylene using atmospheric pressure

discharges," *J. Phys. D. Appl. Phys.*, vol. 36, pp. 666–685, 2003.

[22] J. Kruszelnicki, K. W. Engeling, and J. E. Foster, "Propagation of negative electrical discharges through 2-dimensional packed bed reactors," *J. Phys. D. Appl. Phys.*, vol. 50, p. 25203, 2017.

[23] W. S. Kang, J. M. Park, Y. Kim, and S. H. Hong, "Numerical Study on Influences of Barrier Arrangements on Dielectric Barrier Discharge Characteristics," *IEEE Trans. Plasma Sci.*, vol. 31, no. 4, pp. 504–510, 2003.

[24] A. A. Kulikovsky, "Positive streamer between parallel plate electrodes in atmospheric pressure air," *J. Phys. D. Appl. Phys.*, vol. 30, pp. 441–450, 1997.

[25] H. Russ, M. Neiger, and J. E. Lang, "Requirements for Removal of NO_x from Exhaust Gases," *IEEE Trans. Plasma Sci.*, vol. 27, no. 1, pp. 38–39, 1999.

[26] J. Chang, S. Member, K. G. Kostov, and K. Urashima, "Removal of NF_3 from Semiconductor-Process Flue Gases by Tandem Packed-Bed Plasma and Adsorbent Hybrid Systems," vol. 36, no. 5, pp. 1251–1259, 2000.

[27] K. Takaki, C. Jen-shih, and K. G. Kostov, "Atmospheric Pressure of Nitrogen Plasmas in a Ferro-electric Packed Bed Barrier Discharge Reactor Part I: Modeling," *IEEE Trans. Dielectr. Electr. Insul.*, vol. 11, no. 3, pp. 481–490, 2004.

[28] Y. Uchida, K. Takaki, K. Urashima, and J.-S. Chang, "Atmospheric Pressure of Nitrogen Plasmas in a Ferro-electric Packed-bed Barrier Discharge Reactor Part II: Spectroscopic Measurements of Excited Nitrogen Molecule Density and its Vibrational Temperature," *IEEE Trans. Dielectr. Electr. Insul.*, vol. 11, no. 3, pp. 491–497, 2004.

[29] P. Mehta, P. Barboun, F. A. Herrera, J. Kim, P. Rumbach, D. B. Go, J. C. Hicks, and W. F. Schneider, "Overcoming ammonia synthesis scaling relations with plasma-enabled catalysis," *Nat. Catal.*, vol. 1, no. 4, pp. 269–275, 2018.

[30] K. H. R. Rouwenhorst, H.-H. Kim, and L. Le, "Vibrationally Excited Activation of N_2 in Plasma-Enhanced Catalytic Ammonia Synthesis: A Kinetic Analysis," *ACS Sustain. Chem. Eng*, vol. 7, pp. 17515–17522, 2019.

[31] K. Van Laer and A. Bogaerts, “Fluid modelling of a packed bed dielectric barrier discharge plasma reactor,” *Plasma Sources Sci. Technol.*, vol. 25, p. 015002, 2016.

[32] K. Van Laer and A. Bogaerts, “Influence of Gap Size and Dielectric Constant of the Packing Material on the Plasma Behaviour in a Packed Bed DBD Reactor: A Fluid Modelling Study,” *Plasma Process. Polym.*, vol. 14, pp. 1–11, 2017.

[33] W. Wang, H.-H. Kim, K. Van Laer, and A. Bogaerts, “Streamer propagation in a packed bed plasma reactor for plasma catalysis applications,” *Chem. Eng. J.*, vol. 334, no. September 2017, pp. 2467–2479, 2018.

[34] Y. Uytdenhouwen, S. Van Alphen, I. Michielsen, V. Meynen, P. Cool, and A. Bogaerts, “A packed-bed DBD micro plasma reactor for CO_2 dissociation: Does size,” *Chem. Eng. J.*, vol. 348, no. December 2017, pp. 557–568, 2018.

[35] A. Ozkan, T. Dufour, T. Silva, N. Britun, R. Snyders, A. Bogaerts, and F. Reniers, “The influence of power and frequency on the filamentary behavior of a flowing DBD — application to the splitting of CO_2,” Plasma Sources Sci. Technol., vol. 25, p. 025013, 2016.

[36] A. Ozkan, A. Bogaerts, and F. Reniers, “Routes to increase the conversion and the energy efficiency in the splitting of CO_2 by a dielectric barrier discharge,” *J. Phys. D. Appl. Phys.*, vol. 50, p. 084004, 2017.

[37] A. Ozkan, T. Dufour, A. Bogaerts, and F. Reniers, “How do the barrier thickness and dielectric material influence the filamentary mode and CO_2 conversion in a flowing DBD?,” *Plasma Sources Sci. Technol.*, no. June, p. 45016, 2016.

[38] R. Snoeckx, R. Aerts, X. Tu, and A. Bogaerts, “Plasma-Based Dry Reforming: A Computational Study Ranging from the Nanoseconds to Seconds Time Scale,” *J. Phys. Chem. C*, vol. 117, pp. 4957–4970, 2013.

[39] R. Snoeckx, A. Ozkan, F. Reniers, and A. Bogaerts, “The Quest for Value-Added Products from Carbon Dioxide and Water in a Dielectric Barrier Discharge: A Chemical Kinetics Study,” *ChemSusChem*, vol. 10, pp. 409–424, 2017.

[40] R. Snoeckx, S. Heijkers, K. Van Wesenbeeck, S. Lenaerts, and A. Bogaerts, “CO_2 conversion in a dielectric barrier discharge plasma: N_2 in the mix as a helping hand or problematic impurity?,” *Energy Environ. Sci.*,

vol. 9, pp. 999–1011, 2016.

[41] R. Snoeckx, Y. X. Zeng, X. Tu, and A. Bogaerts, “Plasma-based dry reforming: improving the conversion and energy efficiency in a dielectric barrier discharge,” *RSC Adv.*, vol. 5, pp. 29799–29808, 2015.

[42] R. Snoeckx, M. Setareh, R. Aerts, P. Simon, A. Maghari, and A. Bogaerts, “Influence of N_2 concentration in a CH_4/N_2 dielectric barrier discharge used for CH_4 conversion into H_2,” *Int. J. Hydrogen Energy*, vol. 38, no. 36, pp. 16098–16120, 2013.

[43] R. Aerts, W. Somers, and A. Bogaerts, “Carbon Dioxide Splitting in a Dielectric Barrier Discharge Plasma: A Combined Experimental and Computational Study,” *ChemSusChem*, vol. 8, pp. 702–716, 2015.

[44] R. Aerts, T. Martens, and A. Bogaerts, “Influence of Vibrational States on CO_2 Splitting by Dielectric Barrier Discharges,” *J. Phys. Chem. C*, vol. 116, pp. 23257–23273, 2012.

[45] T. Kozak and A. Bogaerts, “Splitting of CO_2 by vibrational excitation in non-equilibrium plasmas: a reaction kinetics model,” *Plasma Sources Sci. Technol.*, vol. 23, p. 045004, 2014.

[46] G. Colonna, L. D. Pietanza, G. D. Ammando, R. Celiberto, M. Capitelli, and A. Laricchiuta, “Vibrational kinetics of electronically excited states in H_2 discharges,” *Eur. Phys. J. D*, vol. 71, p. 279, 2017.

[47] G. Colonna, A. Laricchiuta, and L. D. Pietanza, “Time dependent selfconsistent electron energy distribution functions during nano-second repetitive discharges in reacting N_2/H_2 mixtures,” *Plasma Phys. Control. Fusion*, vol. 62, p. 014003, 2020.

[48] Y. Teramoto and H.-H. Kim, “Effect of vibrationally excited $N_2(v)$ on atomic nitrogen generation using two consecutive pulse corona discharges under atmospheric pressure N_2,” *J. Phys. D. Appl. Phys.*, vol. 52, p. 494003, 2019.

[49] J. Hong, S. Pancheshnyi, E. Tam, J. J. Lowke, S. Prawer, and A. B. Murphy, “Kinetic modelling of NH_3 production in N_2–H_2 non-equilibrium atmospheric-pressure plasma catalysis,” *J. Phys. D. Appl. Phys.*, vol. 51, no. 10, p. 109501, 2018.

[50] J. Hong, M. Aramesh, O. Shimoni, D. H. Seo, S. Yick, A. Greig, C. Charles, S. Prawer, and A. B. Murphy,

"Plasma Catalytic Synthesis of Ammonia Using Functionalized-Carbon Coatings in an Atmospheric-Pressure Non-equilibrium Discharge," *Plasma Chem. Plasma Process.*, vol. 36, no. 4, pp. 917–940, 2016.

[51] H. Wagner, R. Brandenburg, K. V Kozlov, A. Sonnenfeld, and P. Michel, "The barrier discharge: basic properties and applications to surface treatment," *Vacuum*, vol. 71, pp. 417–436, 2003.

[52] J. Shah, W. Wang, A. Bogaerts, and M. L. Carreon, "Ammonia Synthesis by Radio Frequency Plasma Catalysis: Revealing the Underlying Mechanisms," *ACS Appl. Energy Mater.*, vol. 1, no. 9, pp. 4824–4839, 2018.

[53] S. Pancheshnyi, B. Eismann, G.J.M. Hagelaar, L.C. Pitchford, Computer code ZDPlasKin, http://www.zdplaskin.laplace.univ-tlse.fr (University of Toulouse, LAPLACE, CNRS-UPS-INP, Toulouse, France, 2008).

[54] G. J. M. Hagelaar and L. C. Pitchford, "Solving the Boltzmann equation to obtain electron transport coefficients and rate coefficients for fluid models," Plasma Sources Sci. Technol., vol. 14, pp. 722–733, 2005.

[55] H.-H. Kim and T. Nanba, "Atmospheric-pressure nonthermal plasma synthesis of ammonia over ruthenium catalysts," *Plasma Process. Polym.*, vol. 14, pp. 1–9, 2016.

[56] W. Wang, B. Patil, S. Heijkers, V. Hessel, and A. Bogaerts, "Nitrogen Fixation by Gliding Arc Plasma: Better Insight by Chemical Kinetics Modelling," *ChemSusChem*, vol. 10, no. 10, p. 2110, 2017.

[57] V. Laporta, D. A. Little, R. Celiberto, and J. Tennyson, "Electron-impact resonant vibrational excitation and dissociation processes involving vibrationally excited N_2 molecules," *Plasma Sources Sci. Technol.*, vol. 23, p. 065002, 2014.

[58] I. V Adamovich, J. W. Rich, and C. E. Treanor, "Vibrational Energy Transfer Rates Using a Forced Harmonic Oscillator Model," *J. Thermophys. Heat Transf.*, vol. 12, no. 1, pp. 57–65, 1998.

[59] F. Esposito, "N–N_2 state to state vibrational-relaxation and dissociation rates based on quasiclassical calculations," *Chem. Phys.*, vol. 331, pp. 1–8, 2006.

[60] A. Bogaerts, W. Wang, A. Berthelot, and V. Guerra, "Modeling plasma-based CO_2 conversion: crucial role of the dissociation cross section," *Plasma Sources Sci. Technol.*, vol. 25, p. 055016, 2016.

[61] R. Celiberto, R. K. Janev, J. M. Wadehra, and A. Laricchiuta, "Cross sections for 11-14-eV e–H_2 resonant collisions: Vibrational excitation," *Phys. Rev. A - At. Mol. Opt. Phys.*, vol. 77, no. 1, pp. 1–10, 2008.

[62] R. Celiberto, R. K. Janev, V. Laporta, J. Tennyson, and J. M. Wadehra, "Electron-impact vibrational excitation of vibrationally excited H_2 molecules involving the resonant $^2\Sigma_g^+$ Rydberg-excited electronic state," *Phys. Rev. A - At. Mol. Opt. Phys.*, vol. 88, no. 6, pp. 1–11, 2013.

[63] S. Van Alphen, V. Vermeiren, T. Butterworth, D. C. M. van den Bekerom, G. J. van Rooij, and A. Bogaerts, "Microwave Plasma: A Combined Experimental and Computational Study Power Pulsing to Maximize Vibrational Excitation Efficiency in N_2 Microwave Plasma : A Combined," *J. Phys. Chem. C*, 2019.

[64] M. Capitelli, C. M. Ferreira, B. F. Gordiets, and A. I. Asipov, *Plasma Kinetic in Atmospheric Gases*. Springer 2000.

[65] E. Carrasco, M. Jiménez-Redondo, I. Tanarro, and V. J. Herrero, "Neutral and ion chemistry in low pressure dc plasmas of H_2/N_2 mixtures: Routes for the efficient production of NH_3 and NH_4^+," *Phys. Chem. Chem. Phys.*, vol. 13, no. 43, pp. 19561–19572, 2011.

[66] B. Gordiets, C. M. Ferreira, M. J. Pinheiro, and A. Ricard, "Self-consistent kinetic model of low-pressure N_2-H_2 flowing discharges: I. Volume processes," *Plasma Sources Sci. Technol.*, vol. 7, no. 3, pp. 363–378, 1998.

[67] L. L. Alves, "The IST-LISBON database on LXCat The IST-LISBON database on LXCat," *J. Phys. Conf. Ser.*, vol. 565, p. 012007, 2014.

[68] Morgan database, www.lxcat.net, retrieved on May, 2019.

[69] V. Tarnovsky, H. Deutsch, and K. Becker, "Cross-sections for the electron impact ionization of ND_x (x =1−3)," *Int. J. Mass Spectrom. Ion Process.*, vol. 167–168, pp. 69–78, 1997.

[70] Y. Itikawa, "Cross Sections for Electron Collisions with Nitrogen Molecules," *J. Phys. Chem. Ref. Data*,

vol. 35, no. 1, pp. 31–53, Dec. 2005.

[71] J.-S. Yoon, M.-Y. Song, J.-M. Han, S. H. Hwang, W.-S. C and B. Lee, "Cross Sections for Electron Collisions with Hydrogen Molecules," *J. Phys. Chem. Ref. Data*, vol. 37, no. 2, pp. 913–931, Mar. 2008.

[72] W. L. Nighan, "Electron Energy Distributions and Collision Rates in Electrically Excited N_2, CO, and CO_2," *Phys. Rev. A*, vol. 2, no. 5, pp. 1989–2000, Nov. 1970.

[73] I. A. Kossyi, A. Y. Kostinsky, A. A. Matveyev, and V. P. Silakov, "Kinetic scheme of the non-equilibrium discharge in nitrogen-oxygen mixtures," *Plasma Sources Sci. Technol.*, vol. 1, no. 3, pp. 207–220, 1992.

[74] R. Celiberto, R. K. Janev, J. M. Wadehra, and A. Laricchiuta, "Cross sections for 14-eV e–H_2 resonant collisions: Dissociative electron attachment," *Phys. Rev. A*, vol. 80, no. 1, p. 12712, Jul. 2009.

[75] R. Celiberto, R. K. Janev, J. M. Wadehra, and J. Tennyson, "Dissociative electron attachment to vibrationally excited H_2 molecules involving the $^2\Sigma_g^+$ resonant Rydberg electronic state," *Chem. Phys.*, vol. 398, no. 1, pp. 206–213, 2012.

[76] D. J. Kewley and H. G. Hornung, "Free-piston shock-tube study of nitrogen dissociation," *Chem. Phys. Lett.*, vol. 25, no. 4, pp. 531-536, 1974.

[77] W. Van Gaens and A. Bogaerts, "Kinetic modelling for an atmospheric pressure argon plasma jet in humid air," *J. Phys. D. Appl. Phys.*, vol. 46, no. 27, p. 275201, 2013.

[78] M. A. A. Clyne and D. H. Stedman, "Rate of recombination of nitrogen atoms," *J. Phys. Chem.*, vol. 71, no. 9, pp. 3071–3073, Aug. 1967.

[79] A. Fridman, *Plasma Chemistry*. Cambridge University Press, 2008.

[80] V. G. Anicich, "Evaluated Bimolecular Ion-Molecule Gas Phase Kinetics of Positive Ions for Use in Modeling Planetary Atmospheres, Cometary Comae, and Interstellar Clouds," *J. Phys. Chem. Ref. Data*, vol. 22, no. 6, pp. 1469–1569, 1993.

[81] W. Wang, R. Snoeckx, X. Zhang, M. S. Cha, and A. Bogaerts, "Modeling Plasma-based CO_2 and CH_4 Conversion in Mixtures with N_2, O_2, and H_2O: The Bigger Plasma Chemistry Picture," *J. Phys. Chem. C*,

vol. 122, no. 16, pp. 8704–8723, 2018.

[82] A. Laricchiuta, "The Phys4Entry database," in *GEC12 Meeting of APS*, Austin, Texas, October 22–26, 2012.

[83] R. N. Schwartz, Z. I. Slawsky, and K. F. Herzfeld, "Calculation of Vibrational Relaxation Times in Gases," *J. Chem. Phys.*, vol. 1591, no. May 2013, p. 1591–1599, 1952.

[84] P. J. Chantry, "A simple formula for diffusion calculations involving wall reflection and low density," *J. Appl. Phys.*, vol. 64, no. 4, pp. 1141–1148, 1987.

[85] D. Billing, A. Guldberg, N. E. He, and F. Y. Hansen, "Dissociative chemisorption of N_2 on rhenium: dynamics at low impact energies," *Chem. Phys.*, vol. 147, pp. 1–11, 1990.

[86] F. Y. Hansen, N. E. Henriksen, G. D. Billing, and A. Guldberg, "Catalytic synthesis of ammonia using vibrationally excited nitrogen molecules: theoretical calculation of equilibrium and rate constants," *Surf. Sci.*, vol. 264, no. 1–2, pp. 225–234, 1992.

[87] V. P. Zhdanov, "Arrhenius parameters for rate processes on solid surfaces," *Surf. Sci. Rep.*, vol. 12, no. 5, pp. 185-242, 1991.

[88] J. O. Hirschfelder, C. F. Curtiss, and R. B. Bird, *Molecular theory of gases and liquids*. New York: Wiley, 1954.

[89] A. B. Murphy, "Transport coefficients of plasmas in mixtures of nitrogen and hydrogen," *Chem. Phys.*, vol. 398, pp. 64–72, 2012.

[90] R. A. Svehla and B. J. McBride, "Fortran IV Computer Program for Calculation of Thermodynamic and Transport Properties of Complex Chemical Systems," *NASA Report,* TN-D-7056, 1973.

[91] A. Journal, Z. L. Petrovi, and P. Belgrade, "The Application of Blanc's Law to the Determination of the Diffusion Coefficients for Thermal Electrons in Gases," *Aust. J. Phys.*, vol. 39, no. January 1986, pp. 237–247, 2014.

[92] The Institute of Crystallography – Chemistry of Energy Storage Materials; General chemistry; Structure of Solid; Interstitial sites in close packed lattices, website: minerva.mlib.cnr.it, Accessed on: May 11, 2019.

Electronic Supplementary Information:

Zero-dimensional modelling of unpacked and packed bed dielectric barrier discharges:

The role of vibrational kinetics in ammonia synthesis

K. van 't Veer[1,2], F. Reniers[2], A. Bogaerts[1,*]

[1]*University of Antwerp, Department of Chemistry, Research Group PLASMANT, Universiteitsplein 1, 2610 Wilrijk-Antwerp, Belgium*
[2] *Université Libre de Bruxelles, Faculty of Sciences, Chemistry of Surfaces, Interfaces and Nanomaterials, CP255, Avenue F. D. Roosevelt 50, B-1050 Brussels, Belgium*

[*]E-mail: annemie.bogaerts@uantwerpen.be

Detailed results

1. NH_3 time evolution

Here, we present the modelling results (NH_3 density as a function of time), for a larger variety of number of micro-discharges, showing that the observed trends as discussed in the first part of Section 3.1 are valid over a larger range of conditions.

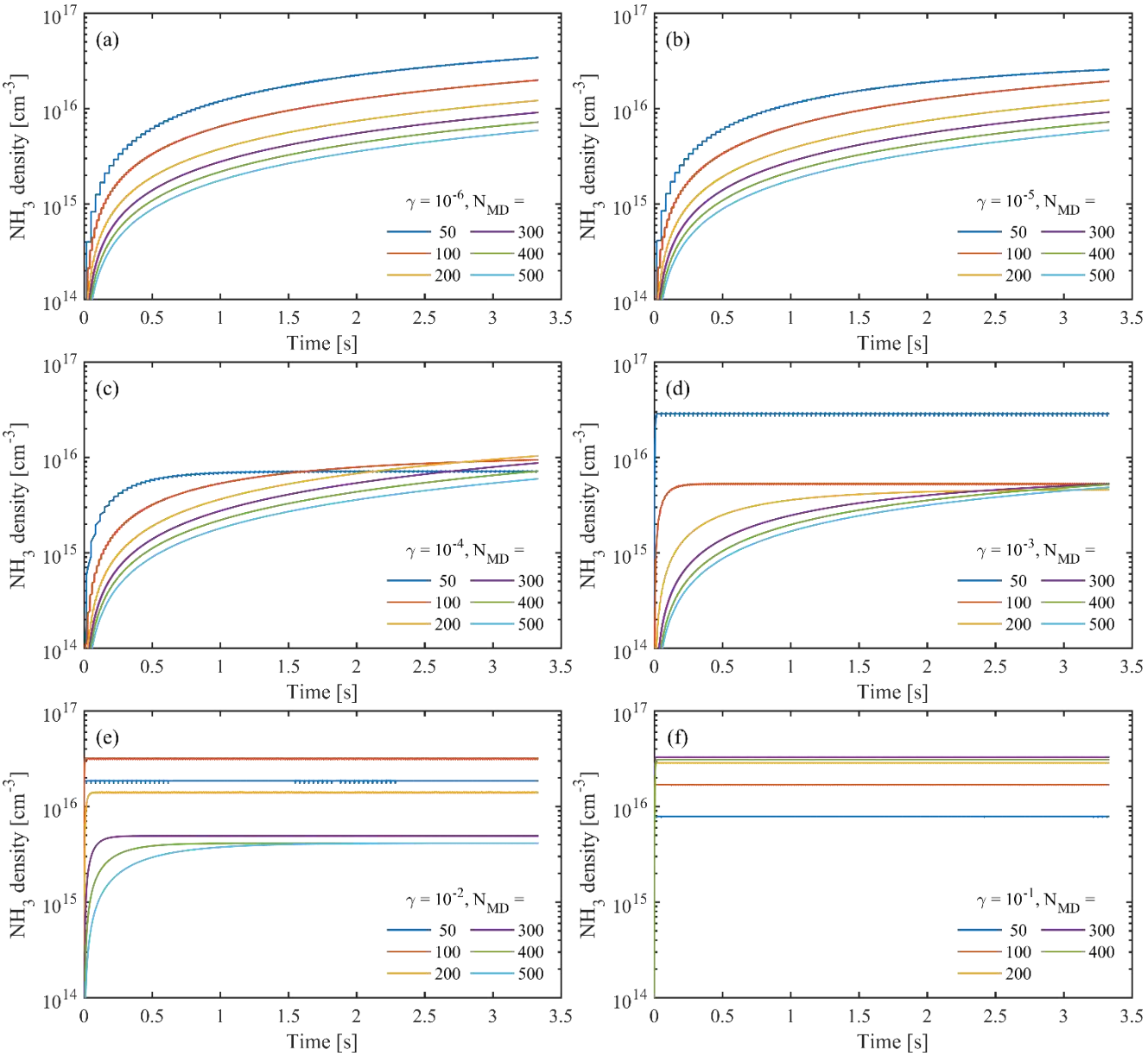

Figure S1. NH_3 density as a function of time for various γ values and number of micro-discharges per half cycle N_{MD} (legend), for the full model, i.e. model (i) (see Section 3.1).

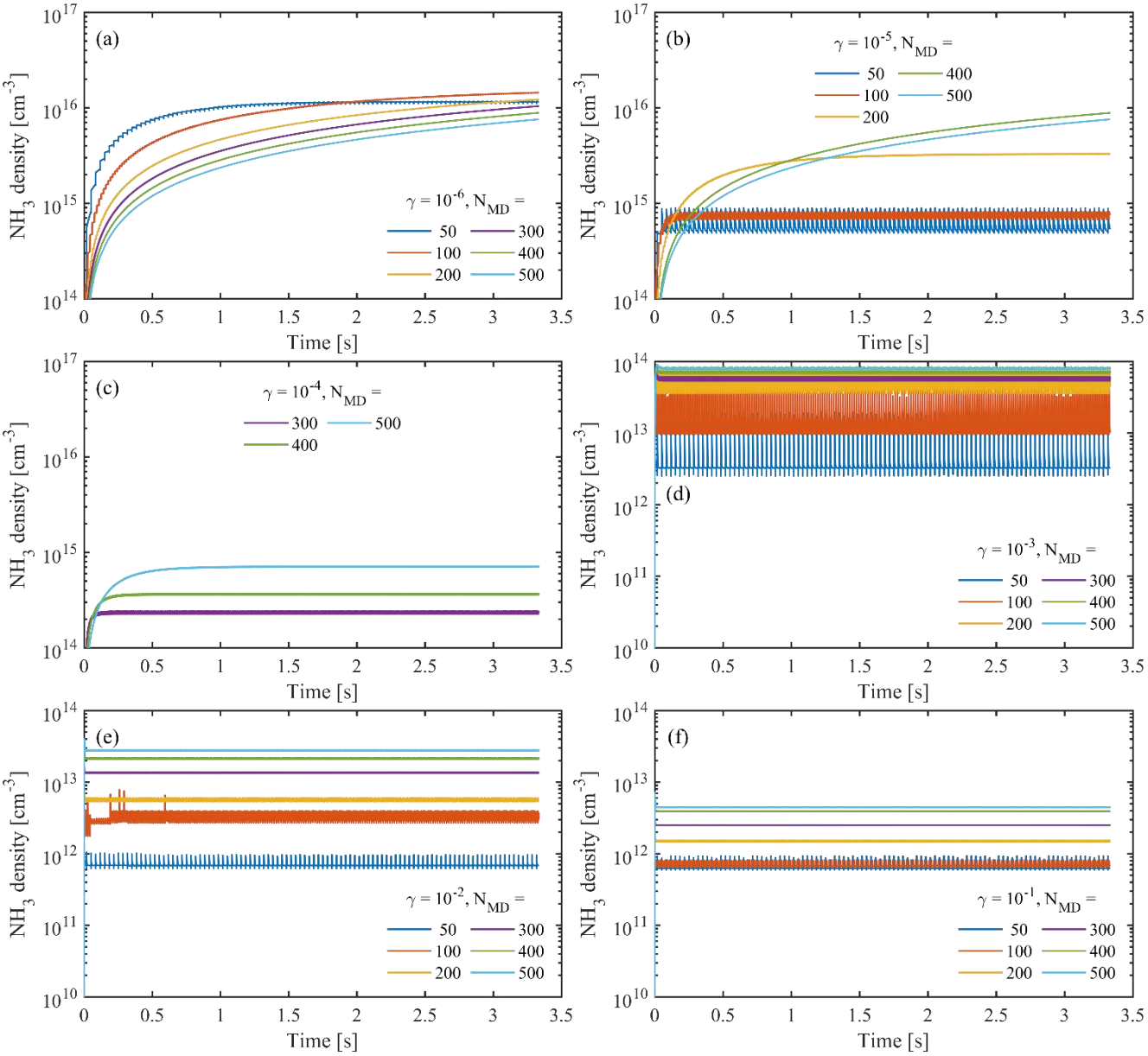

Figure S2. NH_3 density as a function of time for various γ values and number of micro-discharges per half cycle N_{MD} (legend), without vibrational excitation, i.e. model (ii) (see Section 3.1). Note the different scale in the y-axis for (d-f).

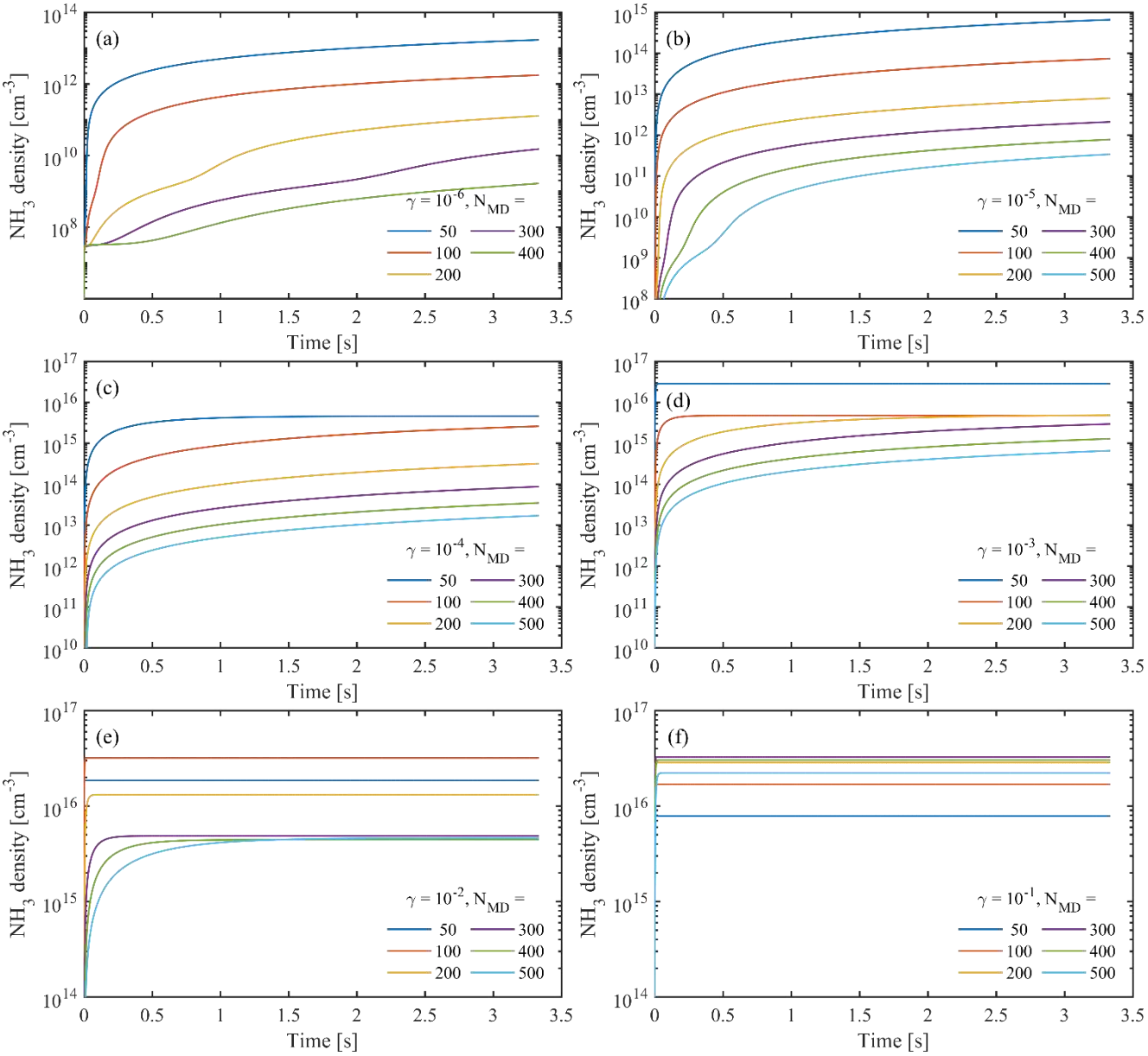

Figure S3. NH_3 density as a function of time for various γ values and number of micro-discharges per half cycle N_{MD} (legend), when neglecting the micro-discharges, i.e., model (iii) (see Section 3.1). Thus, in this figure, γ represents uniform plasma of various strength. The number of micro-discharges influence the strength of the uniform plasma through the definition of the discharge volume (see Appendix C.2). Note the different scale in the y-axis for (a-d).

2. Final NH_3 density

Figure S4 summarizes the final NH_3 density, at the end of the simulations (i.e., after the residence time of 3.33 s), for all models presented in Figures S1 - S3. Figure D.4(a) shows that the full model (i), which includes vibrational excitation, yields a final NH_3 density that varies by less than an order of magnitude for all conditions ($1.4 \pm 1.0 \times 10^{16}$ cm^{-3}), despite significantly different – including very low – amounts of total power effectively felt by the molecules in the 0D model (cf. Figure 1 in the main text).

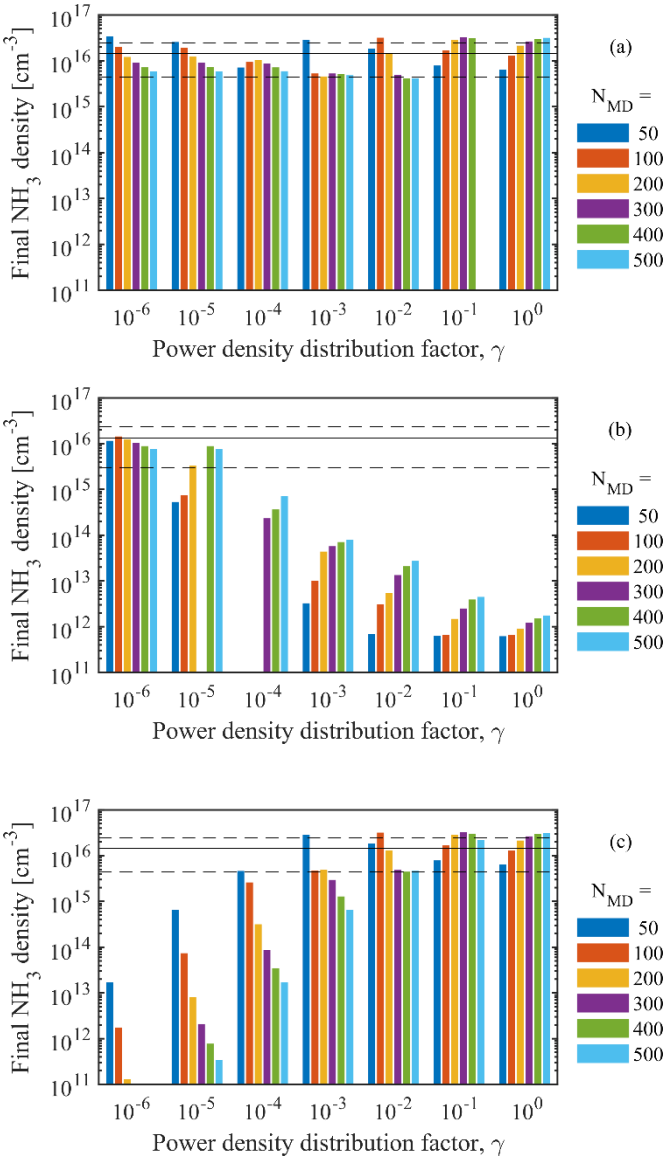

Figure S4. Final (steady state) NH_3 density for various γ values and number of micro-discharges per half cycle N_{MD} (legend), of the full model (a, model (i)), when neglecting vibrational excitation (b, model (ii)), and when neglecting micro-discharges (c, model (iii)) (see Section 3.1). Each figure contains the mean value (solid line) and standard deviation (dashed lines) determined from the various values of γ and N_{MD} in (a), i.e., model (i) that contains vibrational kinetics and micro-discharges.

3. Reduced electric field and vibrational temperature

In Figure S5, the reduced electric field is summarized for a wider range of modelled conditions, analogous to Figure 10. In the filamentary regime ($\gamma = 10^{-6} \ldots 10^{-4}$), the model provides high maximum electric field values for all conditions.

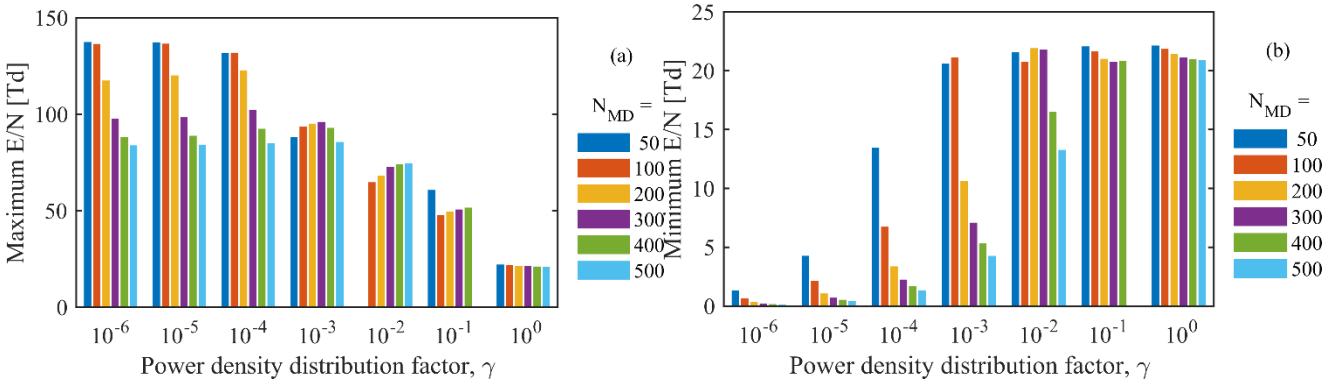

Figure S5. Maximum (a) and minimum (b) reduced electric field (E/N) in the full model (i), as it occurs during the micro-discharges and in between them, respectively, for various γ values and number of micro-discharges per half cycle N_{MD} (legend).

In Figure S6, the N_2 vibrational temperature is summarized for a wider range of modelled conditions, analogous to Figure 11. In the filamentary regime ($\gamma = 10^{-6} \ldots 10^{-4}$), the model predicts high maximum electric field values for all conditions. Sometimes, the vibrational temperature appears to be very similar during and in between the micro-discharges. For example, the temperature varies from 30 K ($N_{MD} = 500$ and all values of γ) to 900 K ($\gamma = 10^{-4}$ and $N_{MD} = 50$) (as reported in section 3.2). This difference is attributed to the time between the pulses, which is smallest for $N_{MD} = 500$ (~ 6 ms) and largest for $N_{MD} = 50$ (~ 60 ms) and the actual power density, which is smaller for $N_{MD} = 500$, due to the definition of the discharge volume (see Appendix C.2).

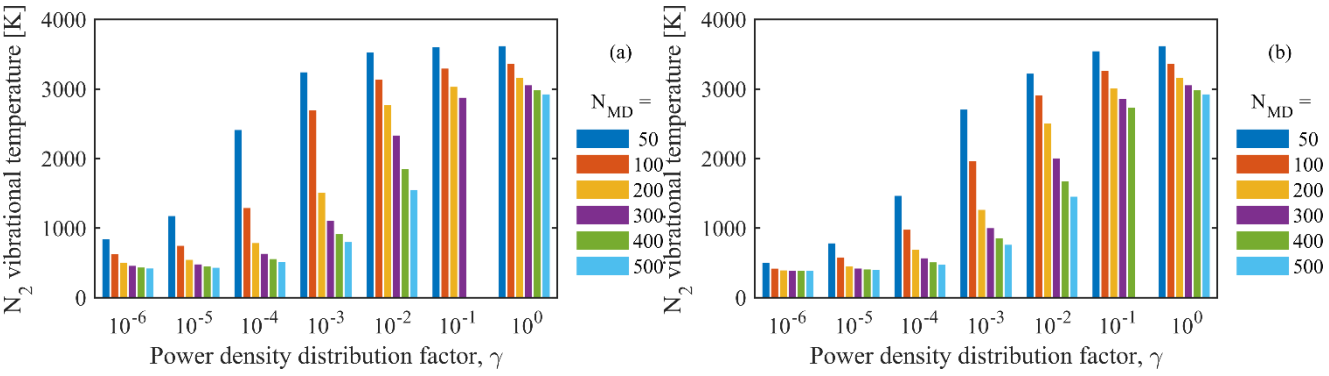

Figure S6. N_2 vibrational temperature in the full model (i), inside the micro-discharges (a) and in between them (b), for γ values and number of micro-discharges per half cycle N_{MD} (legend).